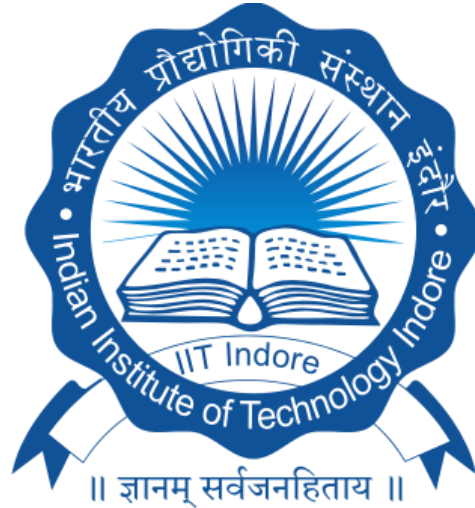


M.Sc. Thesis

**A THEORETICAL DEVELOPMENT OF NOVEL TYPE
PEROVSKITE ELECTROCATALYST**



Submitted by:

Verma Bunty Sardar

M.Sc. physics (1903151023)

Supervisor:

Dr. Srimanta Pakhira

DISCIPLINE OF PHYSICS

INDIAN INSTITUTE OF TECHNOLOGY INDORE

June 2021

A THEORETICAL DEVELOPMENT OF NOVEL TYPE PEROVSKITE ELECTROCATALYST

A THESIS

*Submitted in partial fulfillment of the
Requirements for the award of the degree
Of*

Master of Science

By

Verma Bunty Sardar

(Roll No. 1903151023)

Under the guidance of

Dr. Srimanta Pakhira



DISCIPLINE OF PHYSICS

INDIAN INSTITUTE OF TECHNOLOGY INDORE

June 2021



INDIAN INSTITUTE OF TECHNOLOGY INDORE

CANDIDATE'S DECLARATION

I hereby certify that the work which is being presented in the thesis entitled *A Theoretical Development of Novel Type Perovskite Electrocatalyst* in the partial fulfilment of the requirements for the award of the degree of **MASTER OF SCIENCE** and submitted in the **DISCIPLINE OF PHYSICS, Indian Institute of Technology Indore**, is an authentic record of my own work carried out during the time period from July 2020 to June 2021 under the supervision of **Dr. Srimanta Pakhira, Assistant Professor, DISCIPLINE OF PHYSICS**

The matter presented in this thesis has not been submitted by me for the award of any other degree of this or any other institute.

Bunty
12/06/2021

Signature of the student with date
(Verma Bunty Sardar)

This is to certify that the above statement made by the candidate is correct to the best of my/our knowledge.

17.06.2021

Dr. Srimanta Pakhira
Assistant Professor and Ramonijian Faculty
Discipline of Physics
Indian Institute of Technology Indore
Khandwa Road, Simrol, Indore-453552, MP, India

M.Sc. Thesis Supervisor

(Dr Srimanta Pakhira)

Verma Bunty Sardar has successfully given his/her M.Sc. Oral Examination held on
17th June, 2021.

Convener, DPGC

Date:

24-06-2021

S. Sanal

PSPC Member 1

Date: 18/06/2021

S. Sanal

PSPC Member 2

Date: June 18, 2021

PSPC Member 3

Date: 18/06/2021

Dedicated to My family...

ACKNOWLEDGEMENT

I would like to first say a very big thank you to my supervisor *Dr. Srimanta Pakhira* not only for his support and guidance, but also for giving me the opportunity to undertake this exciting project. His guidance kept me motivated during my work and also helped me in doing a lot of Research and I came to know about so many new things I am really thankful. I am thankful to him for providing necessary information and the direction. He was always there when I was in problem and suggested the right way to move forward. Without him this project was not possible.

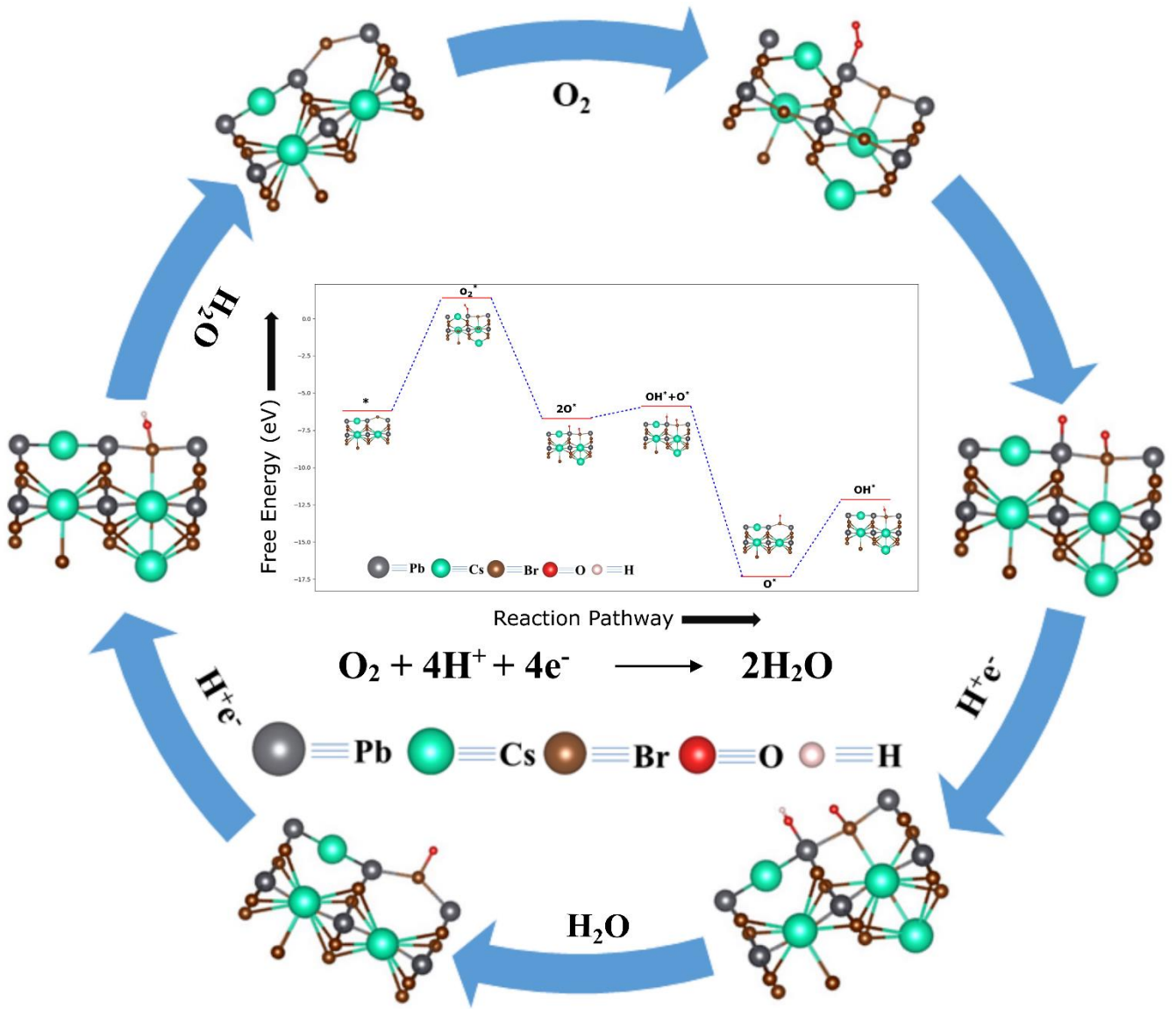
I would also like to thank my PSPC committee members Dr. Sumanta Samal, Dr. Manavendra Mahato and Dr. Sudeshna Chattopadhyay for their support and motivation. I am grateful to all the faculty and HOD and DPGC for the patient guidance, encouragement and advice for his encouraging words and special care during my study period.

I am also thankful to all the members of the *Advanced Computational Materials Science and Theoretical Condensed Matter Physics* group at IIT Indore. I would like to express my thanks to Mr. Shrish Nath Upadhyay and Ms. Nilima Sinha for their moral support and blessings. I would like to thank everyone around me for their kind support. I have no words to express my gratitude for my lab members for their kind help.

This journey would not have been possible without the support of my family, professors and mentors, and friends. To my family, thank you for encouraging me in all of my pursuits and inspiring me to follow my dreams. I am especially grateful to my parents, who supported me emotionally and financially. I always knew that you believed in me and wanted the best for me. Thank you for teaching me that my job in life was to learn, to be happy, and to know and understand myself; only then could I know and understand others. Thank you to my mother, for guiding me as a person, violinist, and teacher and for offering her editing expertise throughout this process.

ABSTRACT

We have studied the CsPbBr₃ type of perovskite material and its application in Oxygen Reduction Reaction (ORR) by using first principles-based hybrid periodic density functional theory (DFT) methods. We have used *ab initio* CRYSTAL17 suite code which makes use of hybrid DFT and studied the material properties from quantum level. We observed that the material showed semiconducting properties, hence not suitable for ORR. So, we doped the material and again performed the DFT calculation to study its electronic structure and properties and after doping transition metal in the pristine CsPbBr₃ it became conductor which is essential for ORR process. A detailed mechanism was done where each important step in the ORR mechanism was explored with a keen insight.



LIST OF PUBLICATIONS

Contents

1	Introduction	11
1.1	What is Perovskite Materials?	11
1.1.1	Perovskite Properties	12
1.1.2	Perovskite Applications	12
1.1.3	Perovskite Solar – panels	13
1.1.4	Challenges of perovskite solar cells	13
1.1.5	Motivation	13
1.2	Perovskite Background	14
1.2.1	Layered Perovskites	15
1.2.2	Tentative classification	16
1.2.3	Common Applications	16
2	Oxygen Reduction Reaction (ORR)	18
2.1	What is Oxygen reduction reaction?	18
2.2	Kinetics of ORR	19
2.3	Electrocatalysts for ORR	21
2.3.1	Single-metal catalyst	22
2.3.2	Metal oxides	23
2.4	Fundamentals and Requirements of a Catalyst	24
2.5	Mechanisms for ORR in the presence of an electrocatalyst	27
3	Computational study of material	30
3.1	What is Density-functional theory?	30
3.1.1	Hohenberg Kohn theorem	34
3.1.2	Kohn-Sham equations	35
3.2	Methodology	38
4	Results and discussions	41
4.1	Reaction Pathway:	44
4.2	Conclusion:	54

List of figures

Figure 1: A schematic of a perovskite crystal structure.	11
Figure 2: Left: Crystal structure of cubic CaTiO_3 . Color code: Ti-blue, Ca-grey, O-red.....	15
Figure 3: Left: Pictorial view of Ruddlesden-Popper phases, with $n=1, 2, 3$ and ∞ . Right: Aurivillius phase, $\text{Bi}_2\text{SrTa}_2\text{O}_9$, two octahedral perovskite layers separated by puckered bismuth oxide sheets (Right).	16
Figure 4: The polarization curve shows the electrochemical efficiency of the PEMFC at any operating current.	21
Figure 5: Oxygen reduction activities as a function of oxygen-binding energy.....	22
Figure 6: Schematic representation of the mechanism of ORR.	24
Figure 7: Trends in oxygen reduction activity plotted as a function of binding energies of (a) O and (b) both the O and the OH on various catalysts.	26
Figure 8: A simplified schematic pathway of oxygen reduction reaction for both acidic and alkaline media.	27
Figure 9: Oxygen reduction on Pt from the (a) bridge model, (b) Griffiths model and (c) Pauling model.	29
Figure 10: Schematic flowchart for finding self- consistent solutions to Kohn- Sham equations.	37
Figure 11: Unit cell CsPbBr_3	40
Figure 12: A 3D Crystal of CsPbBr_3 with band structure and density of states.	42
Figure 13: A 2D monolayer structure of CsPbBr_3 (top view) and (side view) with band structure and density of states.	42
Figure 14: Reaction pathway scheme for ORR.	45
Figure 15: Reaction pathway scheme for ORR.	46
Figure 16: Free energy calculation diagram for ORR pathway on CsPbBr_3	48
Figure 17: A 2D monolayer structure of $\text{O}_2\text{-CsPbBr}_3$ with band structure and density of states.	49
Figure 18: A 2D monolayer structure of 2O-CsPbBr_3 with band structure and density of states.....	49
Figure 19: A 2D monolayer structure of $\text{OH}_2\text{-CsPbBr}_3$ with band structure and density of states.....	50
Figure 20: A 2D monolayer structure of O-CsPbBr_3 with band structure and density of states.....	50
Figure 21: A 2D monolayer structure of OH-CsPbBr_3 with band structure and density of states.....	51
Figure 22: Band structure plot and density of states of each intermediate in the reaction pathway.....	54

List of Table

Table 1: Standard electrode potentials of reactions involved in electrochemical ORR at different pH values in aqueous media.	24
Table 2: The equilibrium lattice parameters of 3D Crystal of CsPbBr_3	40
Table 3: The equilibrium lattice parameters of 3D Crystal and 2D monolayer of CsPbBr_3	43
Table 4: The equilibrium lattice parameters.....	47
Table 5: Change in free energy ΔG (eV) of all reaction steps intermediates of oxygen reduction reaction (ORR) performed on our material CsPbBr_3	48

Chapter 1

1 Introduction

1.1 What is Perovskite Materials?

A perovskite is a material that has the same crystal structure as the mineral calcium titanium oxide, the first-discovered perovskite crystal. Generally, perovskite compounds have a chemical formula ABX_3 , where 'A' and 'B' represent cations and X is an anion that bonds to both. A large number of different elements can be combined together to form perovskite structures. Using this compositional flexibility, scientists can design perovskite crystals to have a wide variety of physical, optical, and electrical properties. Perovskite crystals are found today in ultrasound machines, memory chips, and now in solar cells.

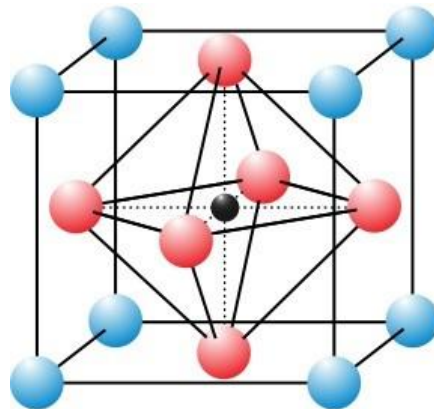


Figure 1: A schematic presentation of a perovskite crystal structure.

The name perovskites have been named after the scientist Lev Perovski who was a mineralogist and it has attracted large attention because of its various properties. There are many perovskite materials and among them, $La_xCa_{1-x}MnO_3$ has huge magnetoresistance property leading to wide functional properties, and $BaTiO_3$ with ferroelectric response had significant impact in this field.¹⁻³ Halide perovskites have also secured applications in photovoltaic performance.⁴ Perovskites are the most

prominent materials for the application in solar cells. The excellent improvement of perovskite solar cells' efficiency has made them the rising star of the photovoltaics world. Recently, optically active Lead halide perovskites has shown promising outcome in various technologies such as LEDs,⁵⁻⁹ high performance solar cells, photodetectors,¹⁰ lasers¹¹⁻¹⁴ etc. These materials have revolutionized the industry for various applications. Some solution processed metal halides have been in talk because of their potential for applications in photoactive materials that will act as next generation high performance optoelectronic material.¹⁵⁻¹⁹ The advancing world is consuming fossil fuels to meet its energy demand more than ever.^{20,21} The overuse of this energy source has led to the depletion of fossil fuels and emission of gases which pollute our environment.^{22,23} To this concern, we have shifted our attention to green energy sources which will be helpful to bring down the greenhouse gas levels and in turn the pollution level of the world. Fuel cells being one of the alternate green energy source has attracted wide span of attention due to its environment friendly attributes and high efficiency. However, there are some limitations associated with it such as corrosion of cathode in fuel cells because of the high operating temperature about 800-1000° C.²⁴ Therefore, the cathode material needs to meet certain requirements such as thermal and chemical stability, good porosity, high electron conductivity, etc.²⁵ As such noble metals such as Platinum do not meet up the expectations because of its limited availability and limited life (vaporization). Certain complex oxides satisfy the above mentioned requirements, among them being PrCoO₃, LaNiO₃, LaMnO₃, LaFeO₃ etc., were used in the solid solution form to enhance conductivity and to be used extensively as the cathodes for solid oxide fuel cells (SOFCs).^{26,27}

1.1.1 Perovskite Properties

Depending on which atoms/molecules are used in the structure, the resulting perovskite can have many different kind properties below.

- Superconductivity
- Giant magnetoresistance
- Spin - dependent transport
- Catalytic properties
- Opto-electronic properties..... And many more.

1.1.2 Perovskite Applications

Perovskite materials exhibit intriguing and unusual physical properties that have been extensively studied for practical applications, theoretical modelling and the materials science and Engineering. The

applications of perovskites became a broad research area with many revolutionary discoveries for new device concepts. Perovskite's potential applications are varied and include uses in sensors and catalyst electrodes, certain types of fuel cells, solar cells, lasers, memory devices and spintronics applications. The most prominent application of perovskites is solar cells. The meteoric improvement of perovskite solar cells efficiency has made them the rising star of the photovoltaics world.

1.1.3 Perovskite Solar – panels

Perovskites are considered as the next-generation solar technology because:

- Low cost
- High efficiency
- Can be printed/sprayed
- Flexible panels
- Transparent panels
- Hybrid Silicon perovskite solar cells
- Perovskites can be integrated into silicon panels, to create highly efficient hybrid panels.

Perovskites are also being studied for many applications like Fuel cells, Lasers, Lens and more.

1.1.4 Challenges of perovskite solar cells

Perovskite solar cells hold massive potential for efficient, low cost solar cells, but this requires overcoming challenges like.

- Stability and lifetime
- Sensitivity to air and moisture
- Toxicity issues (Lead)

1.1.5 Motivation

Transition metal nanoparticles intercalated in graphene layers have presented great stability and activity for ORR. Furthermore, the doping of nitrogen into carbon sites in the carbon layer promotes electron mobility to the adjacent carbon lattice site thereby stimulating great electrocatalytic activity. Various works have been carried out in this regard and still there are only few effective electrocatalysts available for ORR. In this regard, we have worked on the CsPbBr₃ perovskite as a potential efficient electrocatalytic material for ORR. Normally, CsPbBr₃ has three structural phases i.e., cubic, tetragonal and orthorhombic structures. CsPbBr₃ occupies orthorhombic crystal structure at room temperature (around 25°C) and its symmetry changes to cubic around 88°C and to tetragonal at 130°C. So, the structural changes can be induced by heating as per the requirement. Our main focus will be the fundamental understanding of the role played by catalyst in ORR mechanism. The design of cost effective and efficient catalyst for ORR is still a big challenge in fuel cell and renewable energy technology.

1.2 Perovskite Background

Perovskites are materials having the same type of crystal structure as the calcium titanium oxide CaTiO₃ (as depicted in Fig 2), with a general formula of ABO₃. In this structure, an A-site ion, on the corners of the lattice, is usually an alkaline or rare earth element. B site ions, on the centre of the lattice, could be *3d* to *5d* transition metals. Due to interplay between electron, lattice, and spin degrees of freedom, the cubic (undistorted) structure of the CaTaO₃ perovskite is rarely survived: the symmetry is lowered to tetragonal, orthorhombic or trigonal in majority of perovskites. The crystal structure of *Re*TiO₃ (*Re* being a trivalent yttrium or rare-earth ion) is pseudocubic perovskite with strong GdFeO₃-type distortion, which is caused by the tilt of the TiO₆ octahedra, Fig 1 (Right). GdFeO₃-type distortion plays an important role in the electronic and magnetic properties of perovskite titanates *Re*TiO₃. The magnitude of the distortion depends on the ionic radius of the *Re* ion: upon the decrease of ionic radius in the rare-earth series the deviation of the Ti–O–Ti bond angle from 180° occurs, *i.e.*, the lattice distortion increases. Besides the bond length and geometry changes, tilting of the TiO₆ octahedra affects the one-electron bandwidth of the *3d* electron in a way that it gets smaller with the decrease of ionic radius. With the increase of GdFeO₃-type distortion, the magnetic order of Ti changes from *G*-type antiferromagnetic, with the magnetic moment in the direction (LaTiO₃), to ferromagnetic, with the magnetic moment in the *c* direction (YTiO₃).

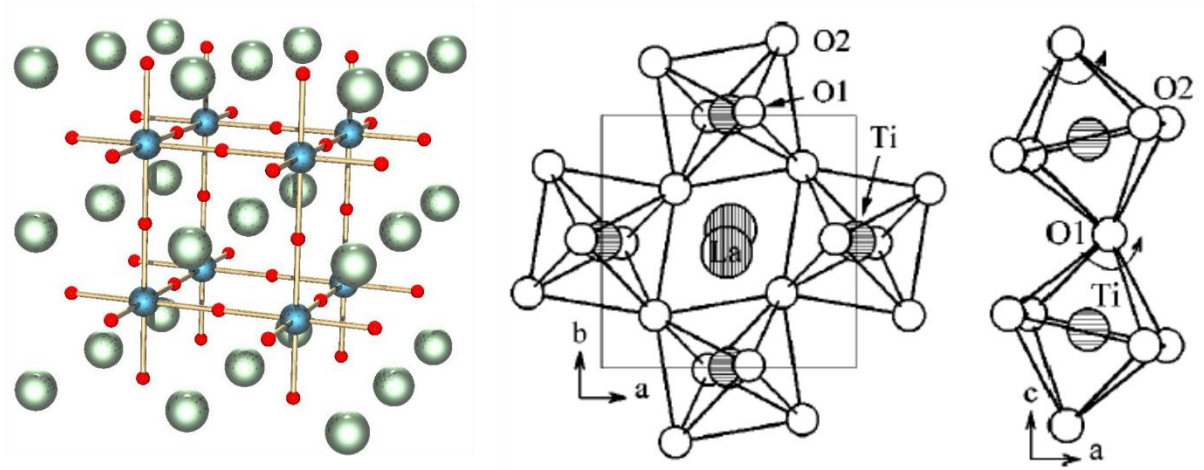


Figure 2: Left: Crystal structure of cubic CaTiO₃. Color code: Ti-blue, Ca-grey, O-red.
Right: Orthorhombic LaTiO₃.

1.2.1 Layered Perovskites

Perovskites may be structured in layers, with the ABO₃ structure separated by thin sheets of intrusive materials. Ruddlesden-Popper (RP) phase has general formula $A_{n-1}A'_2B_nX_{3n+1}$, where A and A' represent alkali, alkaline earth, or rare earth metal, while B refers to transition metal. Aurivillius phase consist of n perovskite-like layers $(A_{n-1}B_nO_{3n+1})^{2-}$ sandwiched between bismuth-oxygen sheets $(Bi_2O_2)^{2+}$.

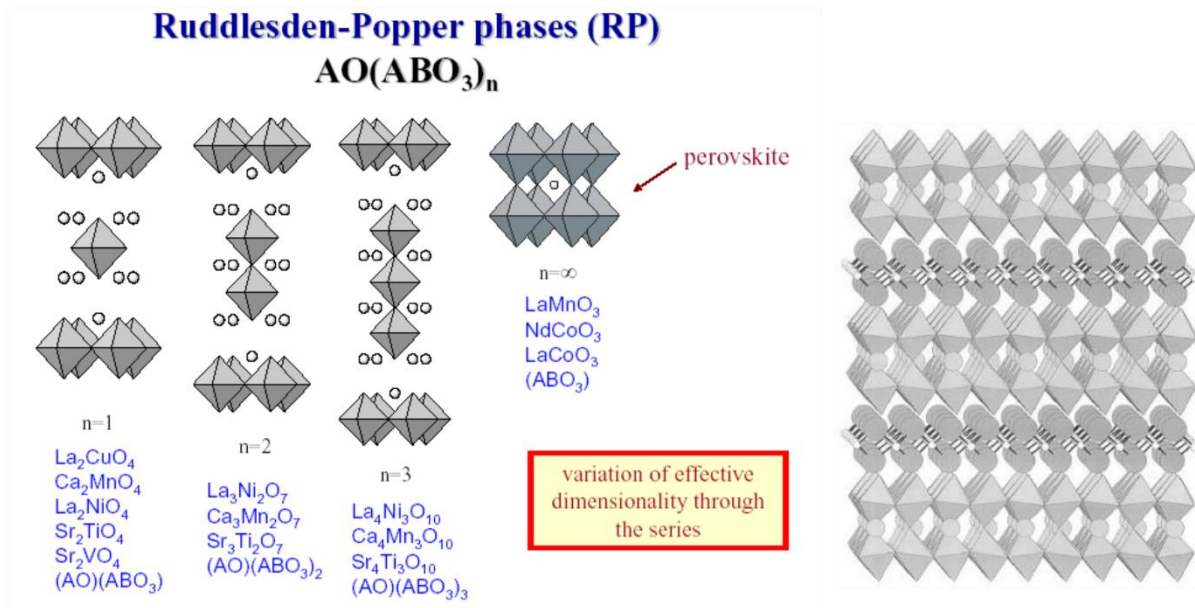


Figure 3: Left: Pictorial view of Ruddlesden-Popper phases, with $n=1, 2, 3$ and ∞ . Right: Aurivillius phase, $Bi_2SrTa_2O_9$, two octahedral perovskite layers separated by puckered bismuth oxide sheets (Right).

1.2.2 Tentative classification

Perovskite materials exhibit many interesting and intriguing properties from both the theoretical and the application point of view. Based on their properties one can tentatively assembly perovskites into the following four groups:

- Superconducting perovskites
- Colossal magnetoresistance perovskites
- Piezoelectric & ferroelectric perovskites
- Other perovskites

1.2.3 Common Applications

In a broad sense, the perovskites are often called, "Functional Materials", due to the interplay of structural, magnetic, and transport properties. Superconductivity, colossal magnetoresistance, and ferroelectricity are discussed in Sects II, III, and IV, respectively. Here we shall list most common applications for other perovskites:

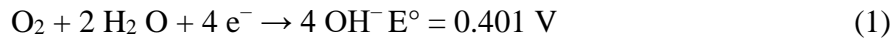
- (a) Thermopower generation;
- (b) Ion conductors in fuel cells/sensors;
- (c) Catalytic materials and Co-based perovskite material is as a replacement for Pt in catalytic converters in diesel vehicles;
- (d) Photovoltaics and synthetic perovskites have been identified as possible inexpensive base materials for high-efficiency commercial purposes. The conversion efficiency of perovskite solar cells leaped from just a few percent in 2010 to more than 16% in current versions. The fast-paced improvement, which hasn't shown signs of slowing, coupled with inexpensive materials and preparation methods indicates that perovskite solar cells are poised "to break the prevailing paradigm" by combining low cost and excellent performance.

Chapter 2

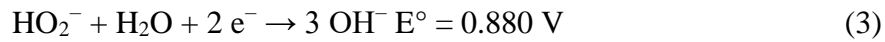
2 Oxygen Reduction Reaction (ORR)

2.1 What is oxygen reduction reaction?

Oxygen reduction reaction (ORR)²⁸ is an important topic of investigation in last century because ORR has been of utmost importance in area of energy conversion and fuel cells.²⁹ ORR is an important cathodic process in polymer electrolyte membrane fuel cells.^{30–36} Among many available catalysts, Pt is still the best catalyst for ORR due to zero overpotential, but the major problem is that Pt is rare and expensive and hence major research is being conducted to find alternate electrocatalysts.^{37,38} At present, most of the energy demands of the community are being satisfied by the conventional energy sources. Scientists and researchers are in search of some green and renewable energy sources to fulfil the energy demands of society. In this step, ORR is one of the most important reactions in energy conversion. It has been the subject of large-scale exploration over the last century. These are the most encouraging solutions for the future energy demands in various applications like electric vehicles and fuel cells. Fuel cells are the technologies used for the conversion of chemical energy into electricity by electrochemical reactions.³⁹ ORR are well studied cathodic reactions in fuel cells. Oxygen reduction in aqueous solutions occurs mainly through two different pathways: either a four-electron reduction pathway from O_2 to H_2O or a two-electron pathway from O_2 to H_2O_2 .⁴⁰ The most accepted mechanism of ORR was first proposed by Damjanovic et al.^{41,42} and later modified by Wroblowa et al.,⁴³ making it easier to understand the complicated reaction pathway of oxygen on the metal surface. They suggest that ORR proceeds along two parallel reaction pathways with rates that are comparable. In Proton-exchange membrane fuel cells (PEMFC), a four-electron transfer is preferred and energetically more favourable. The ORR is alkaline media versus reversible hydrogen electrode (RHE) at 25°C, and its thermodynamic potentials at standard conditions are presented as follows:⁴⁴

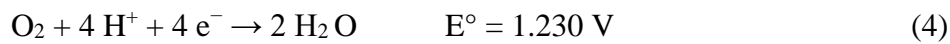


The pathway involving the hydrogen peroxide is expressed as follows:

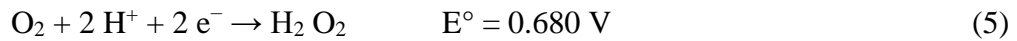


The ORR is acidic media versus RHE at 25°, and its thermodynamic potentials at standard Conditions are presented as follows:

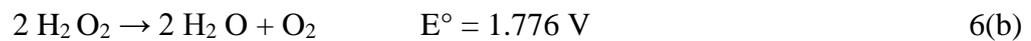
Direct four-electron reduction



Indirect reduction:



Or chemical decomposition:



2.2 Kinetics of ORR

It is desirable for the ORR to occur at potentials close to thermodynamic potentials as much as possible. For the thermodynamic potentials to be obtained, the charge transfer kinetics of the ORR must be quick. It has been reported that the kinetics of fuel cells at cathode are slow, hence show over-potential η as in Eq. (7):

$$\eta = E - E_{eq} \quad (7)$$

E is the resultant potential and E_{eq} is the equilibrium potential.

The difference between E and E_{eq} is called polarisation.

There are three distinct types of polarisation expressed in Eq. (8):

$$\eta = \eta_{act} + \eta_{conc} + iR \quad (8)$$

η_{act} is the activation over-potential, a function describing the charge transfer kinetics of an electrochemical reaction. η_{act} is always present and mostly dominant at small polarisation currents. η_{conc} is the concentration over-potential, a function describing the mass transport limitations associated with electrochemical processes. η_{conc} is predominant at larger polarisation currents. iR is the Ohmic voltage drop. This function takes into account the electrolytic resistivity of an environment when the anodic and cathodic elements of a corrosion reaction are separated by this environment while still electrically coupled. Figure 1 depicts a polarisation curve showing the electrochemical efficiency of a fuel cell. The expression relating the over-potential, η , and the net current is known as the Butler-Volmer equation and is given as follows:

$$i = i_0 \left\{ \exp\left(\beta \frac{nF}{RT} \eta\right) - \exp\left(-[1 - \beta] \frac{nF}{RT} \eta\right) \right\} \quad (9)$$

where i is the ORR current density, i_0 is the exchange current density, n is the number of electrons transferred in the rate-determining step, β is the transfer coefficient.

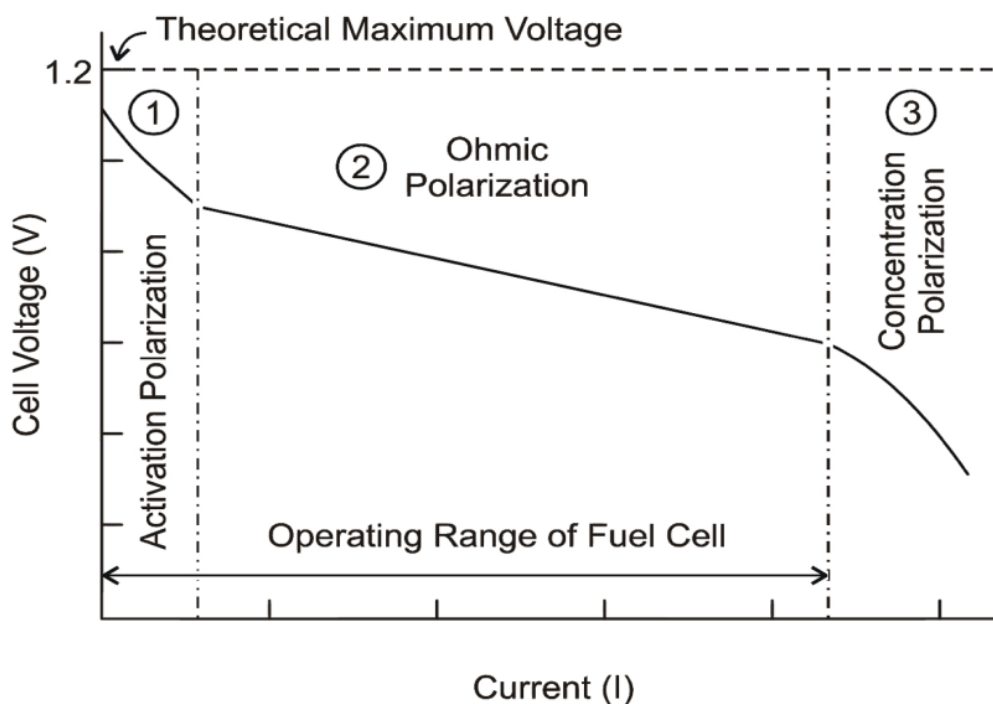


Figure 4: The polarization curve shows the electrochemical efficiency of the PEMFC at any operating current.

2.3 Electrocatalysts for ORR

The kinetics of the ORR at the cathode are very important, as they are the factors for the performance of PEMFCs.⁴⁵ There are several issues that need to be addressed, including slow reaction kinetics at the cathode, which are due to highly irreversible ORR, and fuel crossover in the cathode, which causes a mixed potential, leading to potential loss and 25% reduction in efficiency, hence reducing the ORR performance.⁴⁶⁻⁴⁸ An electrocatalyst is used to induce a four-electron reduction of O_2 to water by utilising the protons that permeate from the anode. Pt is the excellent electrocatalyst which is currently used for ORR reactions, as it is the only commercially available catalyst with sensible activity and stability for PEMFCs, although it offers limited commercialisation of fuel cells due to its limited availability and high cost.⁴⁹ It is also reported that Pt still shows over-potentials of over 400 mV from the equilibrium reversible potentials (1.19 V at 80°C).⁵⁰ These high potentials result in the formation of adsorbed species on a platinum surface that restrain the ORR and hence result in performance loss. Considerable research has been conducted to try to reduce the costs of fuel cells, which is one of the stumbling blocks in fuel cell commercialisation using low-cost non-Pt catalysts such as supported platinum group metals Pd, Ir and Ru; improve the electrocatalytic activity of the cathode catalyst, which includes using bimetallic alloy catalysts, transition metal macrocyanides, transition metal chalcogenides and metal oxides in order to

improve the ORR kinetics on the new catalyst; and fabricate Pt with novel nanostructures such as nanotubes, graphene and carbon nanofibres (CNFs), as it is known that supports may significantly affect the performance of the catalyst. However, these efforts are still in the research stage, as their activity and stability are still lower than that of the Pt catalyst.

2.3.1 Single-metal catalyst

Other noble metals, such as Pd, Ag, Rh, Ir and Ru, have also been used as cathode materials for ORR.⁵¹ Among these, Pd has the same electron configuration and lattice constant as Pt, as they belong to the same row in the periodic table, showed the most improved ORR towards alcohol in an alkaline medium, while it is reported to be inactive in an acidic medium.⁵² It has been showed that Pd/C is less sensitive to alcohol contamination compared to Pt/C, hence more tolerant to alcohol crossover.^{53,54} However, when comparing the ORR activity of Pd/C to Pt/C, the former has less activity and high potentials of amount 0.8 V versus NHE, hence less stability, which prevents its replacement as the preferred ORR catalyst over Pt/C.⁵⁵ The noble metals in terms of ORR activity follow the trend: Pt > Pd > Ir > Rh.⁵⁶ Wang reports that Ru can undergo a four-electron reduction reaction. Ag is reported

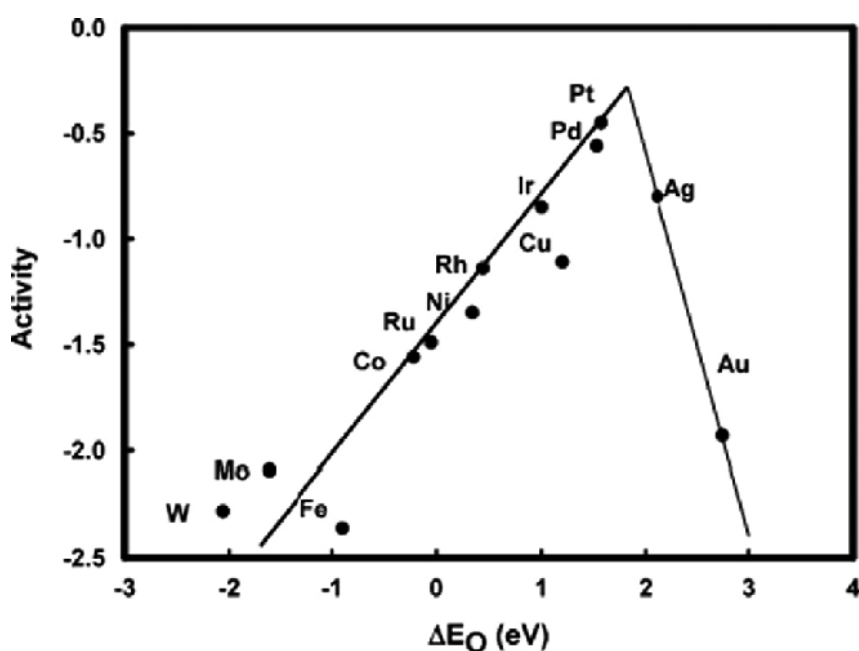


Figure 5: Oxygen reduction activities as a function of oxygen-binding energy.

to show less electrocatalytic activity towards ORR compared to Pt but is more stable than Pt cathodes during long-term operations.

There are several metals other than noble metals which were also evaluated as cathode catalysts for ORR. Figure 5 shows a comparison of the activities of various catalysts as a function of binding energy. These catalysts showed less catalytic activity towards ORR compared to Pt, with less electrochemical stability.⁵⁷

2.3.2 Metal oxides

Another route to stabilising nanoparticles is the development of metal oxide composite supports. Metal oxides such as IrO₂, NiO, CeO₂, ZrO₂, TiO₂ and SnO₂ have also been studied as ORR catalysts in basic acidic media.⁵⁸⁻⁶¹ Nanoparticles on metal oxides are not able to improve the electrocatalytic activity due to their limited electron conductivity, but are reported to have excellent corrosion resistance in various electrolyte media.^{62,63} Researchers use metal oxides in combination with carbon supports that have desirable properties such as a high surface area and a high electric conductivity. The metal oxides combined with carbon supports are reported to improve the stability and the electrocatalytic activity of the electrode material. Carbon surfaces are functionalised before they are used as supports for catalysts in order to improve their surface properties, but the disadvantage of functionalisation is that it accelerates the degradation process of the support material. The presence of the metal oxide delays the corrosion process. Montero-Ocampo et al. report on PtTiO₂ and PtTiO₂/CNT synthesised using metal organic chemical vapour deposition. The PtTiO₂/CNT was more electrocatalytically active compared to PtTiO₂, while good stability was observed for both PtTiO₂ and PtTiO₂/CNT that was provided by the TiO₂ support. This was attributed to the high conductivity of CNT compared to TiO₂, which has limited electron conductivity. Pt/TiO₂/C showed improvement in activity and thermal stability for ORR compared to Pt/C. Khotseng et al.⁶⁴ compared the activity for PtRu/TiO₂ to commercial PtRu/C and Pt/C. They reported a high electroactive surface area and activity of commercial Pt/C and PtRu/C compared to PtRu/TiO₂ towards ORR. When durability studies were performed for the same catalysts, the PtRu/TiO₂ recorded a loss of 29% compared to Pt/C and PtRu/C, which recorded a loss of 64 and 32%, respectively. Li et al.⁶⁵ reported an improved oxygen reduction activity, a better durability and a higher methanol tolerance capability in alkaline solution compared to Pt/C. Most of the metal oxides were found to be unstable in acidic media. To overcome this instability, conducting polymer polypyrrole (Ppy) was used against the dissolution of metal oxides. During synthesis, the metal oxides were sandwiched between the Ppy layers. Through this research, an improved electrochemical stability of the metal oxides was achieved. Singh et al.⁶⁶ report on CoFe₂O₄ oxides sandwiched between Ppy layers. A high electrocatalytic activity towards ORR at high cathodic potentials was obtained with stability in acidic media.

2.4 Fundamentals and Requirements of a Catalyst

Electrochemical ORR mechanism is quite complex and involves many intermediates depending upon the nature of the electrode material, electrocatalyst, electrolyte and the solvent used. As mentioned above, ORR takes place by either a 4-electron pathway or a 2-electron pathway in aqueous media.⁶⁷⁻⁶⁹ the mechanism involves adsorption of molecular O_2 on to the electrocatalyst surface followed by the activation of O–O bond and subsequent cleavage to produce adsorbed atomic O on the electrode surface. This results in H_2O as the product either in a direct 4-electron pathway or in two consecutive steps of two electrons each (4-electron process). On the other hand, if the

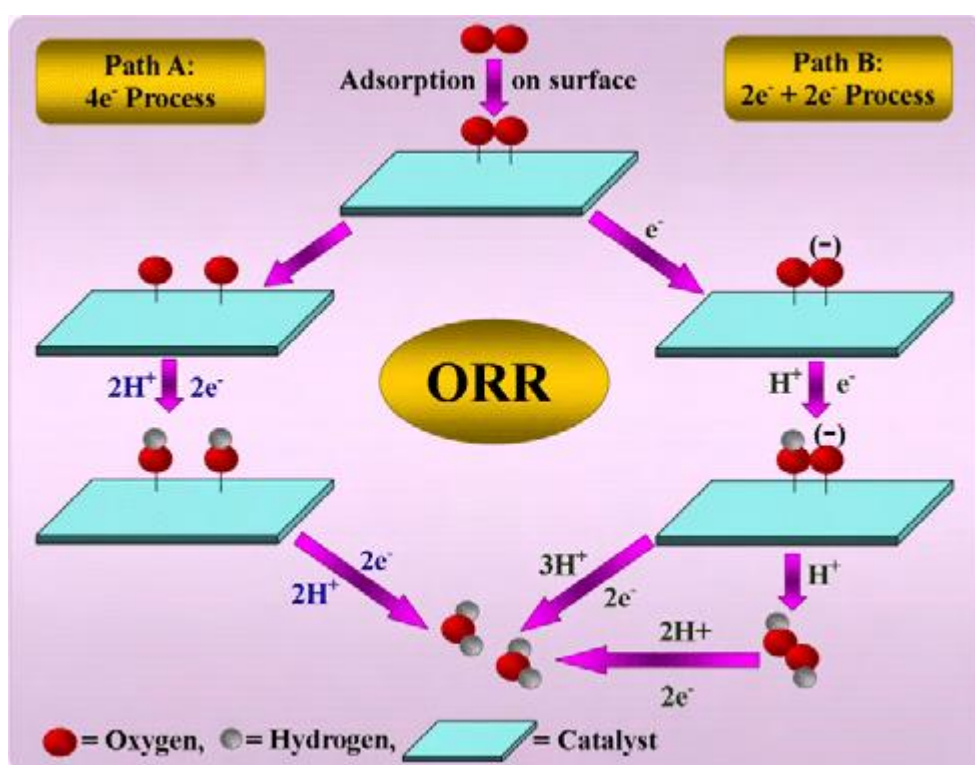


Figure 6: Schematic representation of the mechanism of ORR.

Table 1: Standard electrode potentials of reactions involved in electrochemical ORR at different pH values in aqueous media.

Electrolyte	Reaction	Standard potential/V
Aqueous acidic	$O_2 + 4H^+ + 4e^- \rightarrow 2H_2O$	1.229
	$O_2 + 2H^+ + 2e^- \rightarrow H_2O_2$	0.70
	$H_2O_2 + 2H^+ + 2e^- \rightarrow 2H_2$	1.76
Aqueous alkaline	$O_2 + 2H_2O + 4e^- \rightarrow 4OH^-$	0.401
	$O_2 + H_2O + 2e^- \rightarrow HO_2^- + OH^-$	-0.065
	$HO_2^- + H_2O + 2e^- \rightarrow 3OH^-$	0.867

adsorbed molecular oxygen does not undergo O–O bond cleavage, the product stops at peroxide (2-electron transfer) stage. Figure 3.2.1 gives a schematic representation of ORR mechanisms in aqueous media.

The standard electrode potential values for ORR in aqueous media at different pH values are given in Table 1. An essential requirement for a heterogeneous catalyst-based on Sabatier principle is that the electrocatalyst should bind the key intermediate strong enough so that the reagents will likely bind and

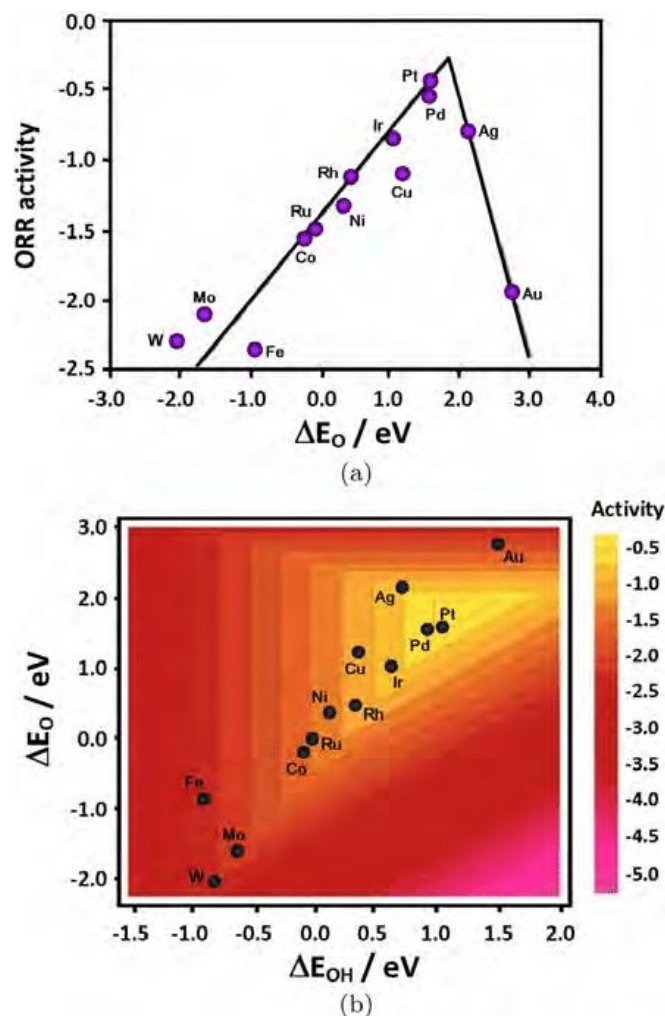


Figure 7: Trends in oxygen reduction activity plotted as a function of binding energies of (a) O and (b) both the O and the OH on various catalysts.

react, but weak enough so that the product will easily desorb. In other words, the catalyst should be thermoneutral with respect to the reaction concerned. Hence, it is important to find out the adsorption ability of the catalysts to various species involved in the reaction. Figure 7(a) shows the plot of activity for ORR vs. binding energy for various metallic catalysts towards oxygen. It should, however, be pointed out that the adsorption of various intermediates is to be taken into account in predicting the activity. Particularly, for a multi-electron transfer reaction such as ORR, it is quite important to understand the coverages of various species since the surface concentration (coverage, θ) would determine the adsorption parameters such as ΔH and ΔG values.

2.5 Mechanisms for ORR in the presence of an electrocatalyst

Oxygen reduction on Pt is one of the most extensively studied mechanisms. It involves a multi-electron process with a number of elementary steps, involving different reaction intermediates. The mechanism can be shown schematically as follows⁷⁰ as shown in Figure 8. From the mechanism, only two products are observed with ORR on Pt, either H₂O, which can directly form through a four-electron reduction with the rate constant k_1 , or adsorbed hydrogen peroxide (H₂O₂, ads), which is through a two-electron process with the rate constant k_2 , which can be reduced further by another two-electron process to form water with rate

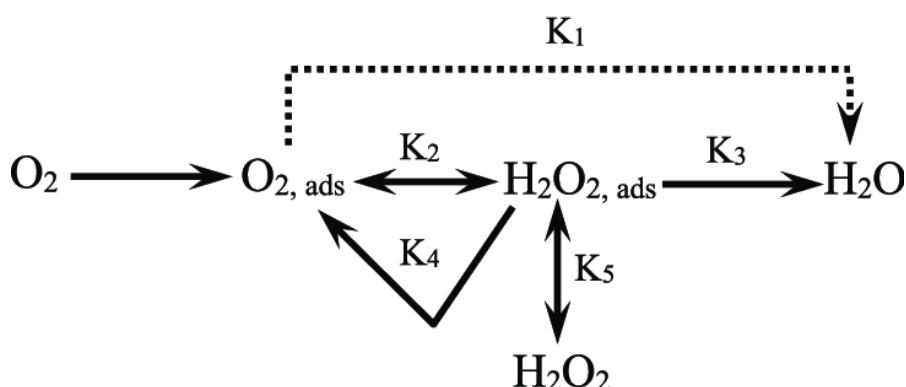
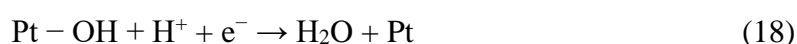


Figure 8: A simplified schematic pathway of oxygen reduction reaction for both acidic and alkaline media.

Constant k_3 , or be chemically decomposed on the electrode surface (k_4), or be desorbed in the electrolyte solution (k_5). For ORR in fuel cells, the direct four-electron process is required. Oxygen reduction on a Pt catalyst in acid media occurs via dissociative adsorption of O₂ followed by the protonation of the adsorbed species, with the former being the rate-determining step. The main steps in the mechanism of ORR are given subsequently. One is known as dissociative mechanism for a low current density range and the other associative mechanism for a high current density range:

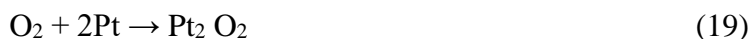
Dissociative mechanism:



In this mechanism, no H₂O₂ is formed. On the Pt surface, the O₂ adsorption breaks the O—O bond and forms adsorbed atomic O with further gain of two electrons, in the two consecutive steps, forming H₂O.

Because there is no adsorption of O₂ on the surface, no H₂O₂ can be formed. This mechanism can be considered as the direct four-electron reduction reaction.

Associative mechanism:



In this mechanism, no H₂O₂ is involved as well. Because there is adsorbed O₂ on the surface, O—O may not be broken down in the following steps, resulting in the formation of H₂O₂, which can be reduced further to form water. Pt shows two Tafel slope regions. At a high potential, low current density (>0.8 V), the electrode surface is a mixture of Pt and PtO with the Tafel slope of 60 mV dec⁻¹ and the reaction order 0.5 with respect to pH in alkaline media. The fractional reaction order was represented in terms of the first electrochemical step as a rate-determining step under the Temkin isotherm, that is, the adsorption of reaction intermediates O_{ads}, OH_{ads} and HO_{2ads}.^{71,72}

The rate expression under Temkin conditions of adsorption is

$$j = k [O_2] [H^+]^{1/2} \exp [- \eta F / RT] = 374 k [O_2] [OH^-]^{1/2} \exp [- \eta F / RT] \quad (24)$$

Where k is the rate constant and η is the over-potential.

At a low potential, high current density (<0.8 V), the electrode surface is a pure Pt with the Tafel slope of 120 mV dec⁻¹ and the reaction order 0 with respect to pH in alkaline media, with H₂O as the reacting species. The adsorption of intermediate species to a Langmuir isotherm under Temkin conditions no longer holds.

The rate expression under Langmuir conditions is

$$j = k [O_2] \exp [- \beta \eta F / RT] \quad (25)$$

where β is the symmetry factor.

The reaction is of the first order with respect to O_2 in solutions. It was found that the H_2O_2 formed was greater in an alkaline solution than in an acidic one. In alkaline solutions, about 80% of the reduction current is through the direct reduction and the other current forms H_2O_2 , which leads to a complicated mechanism.

Various models representing the adsorbed states of oxygen are represented in Figure 9.

Figure 9(a) is known as the bridge model. It is a 2:2 complex of metal oxygen where the bonding arises from the interaction between the d-orbital on the metal with a Π^* and Π orbital combination on O_2 . This gives rise to a singlet or a triplet nature of di-oxygen orbitals.

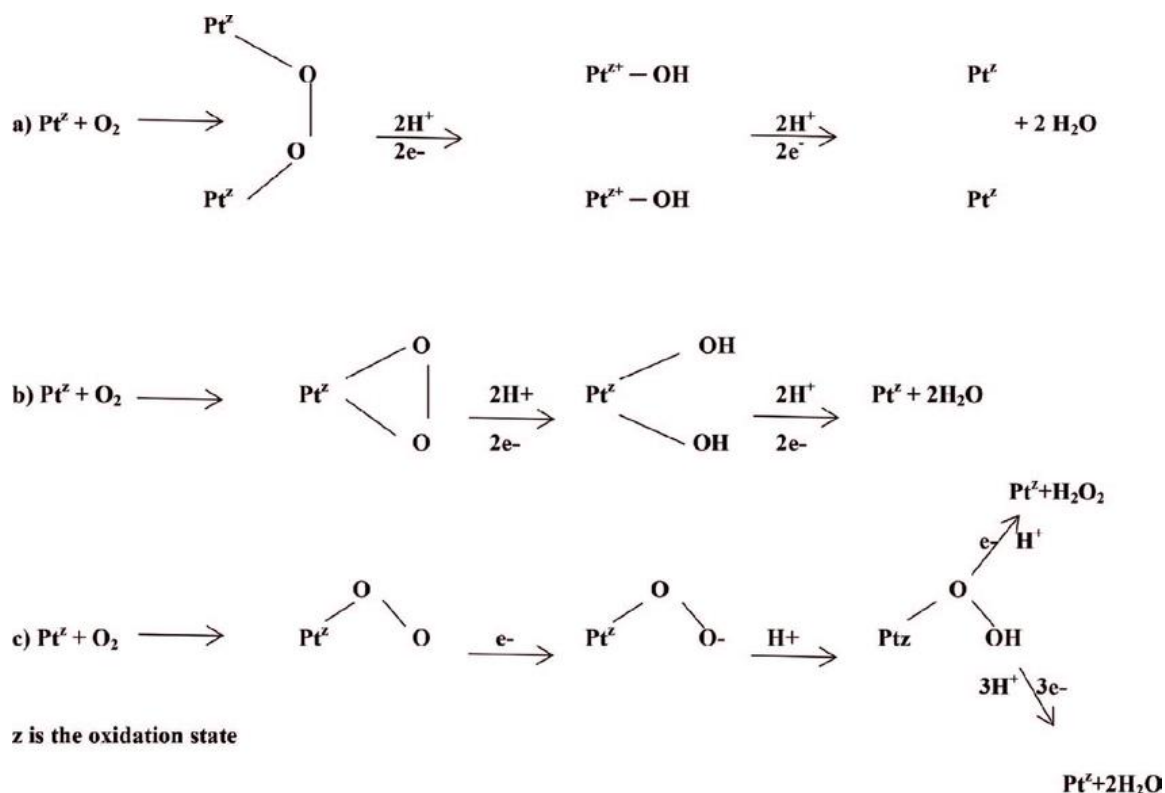


Figure 9: Oxygen reduction on Pt from the (a) bridge model, (b) Griffiths model and (c) Pauling model.⁷³

and determines the bridge or a transmode of interaction of di-oxygen with the metal.⁷⁴ Figure 9(b) is known as the Griffiths model. It is a 2:1 metal-di-oxygen complex structure, which involves a side on the interaction of oxygen with metal. This type of bonding can be viewed as rising from two contributions: (1) σ -type bonding is formed by overlapping between the Π orbitals of oxygen and the d_{z^2} orbitals on the metal; (2) Π back-bond interaction between the metal d- Π orbitals and partially occupied Π^* antibonding orbital on O_2 arises.⁷⁵ Figure 9(c) is known as the Pauling model. It is a 1:1 metal-oxygen complex structure, which is an end-on interaction of O_2 with metal. In this model, the σ bond is formed by the

donation of electron density from the σ -rich orbital of di-oxygen to the acceptor d_z^2 orbital on the metal. The metal's two d orbitals, namely d_{xz} and d_{yz} , then interact with the Π^* orbitals of di-oxygen, with the corresponding charge transfer from the metal to the O_2 molecule. The Griffiths and Pauling models are the preferred models due to the donating abilities of the filled Π and σ orbitals of the di-oxygen molecule, respectively.

Chapter 3

3 Methodology

3.1 What is Density-functional theory?

Density-functional theory is one of the most popular and successful quantum mechanical approaches to matter. It is nowadays routinely applied for calculating, e.g., the binding energy of molecules in chemistry and the band structure of solids in physics. First applications relevant for fields traditionally considered more distant from quantum mechanics, such as biology and mineralogy are beginning to appear. Superconductivity, atoms in the focus of strong laser pulses, relativistic effects in heavy elements and in atomic nuclei, classical liquids, and magnetic properties of alloys have all been studied by applying the DFT.

DFT owes this versatility to the generality of its fundamental concepts and the flexibility one has in implementing them. In spite of this flexibility and generality, DFT is based on quite a rigid conceptual framework. This section introduces some aspects of this framework in general terms. The following two sections, 3 and 4, then deal in detail with two core elements of DFT, the Hohenberg-Kohn theorem and the Kohn-Sham equations. The final two sections, 5 and 6, contain a (necessarily less detailed) description of approximations typically made in practical DFT calculations, and of some extensions and generalizations of DFT.

To get a first idea of what density-functional theory is about, it is useful to take a step back and recall some elementary quantum mechanics. In quantum mechanics, we learn that all information we can possibly have about a given system is contained in the system's wave function, Ψ . Here, we will

exclusively be concerned with the electronic structure of atoms, molecules and solids. The nuclear degrees of freedom (e.g., the crystal lattice in a solid) appear only in the form of a potential $v(r)$ acting on the electrons, so that the wave function depends only on the electronic coordinates.⁷⁶ Nonrelativistically, this wave function is calculated from Schrödinger's equation, which for a single electron moving in a potential $v(r)$ reads

$$\left[-\frac{\hbar^2 \Delta^2}{2m} + v(r) \right] \psi(r) = \epsilon \psi(r) \quad (1)$$

If there is more than one electron (i.e., one has a many-body problem)

This is the so-called Born-Oppenheimer approximation. It is common to call $v(r)$ a 'potential' although it is, strictly speaking, a potential energy.

Schrödinger's equation becomes

$$\left[\sum_i^N -\frac{\hbar^2 \Delta_i^2}{2m} + v(r_i) + \sum_{i<j} U(r_i, r_j) \right] \psi(r_1, r_2 \dots r_N) = E \psi(r_1, r_2 \dots r_N) \quad (2)$$

Where N is the number of electrons and $U(r_i, r_j)$ is the electron-electron interaction. For a Coulomb system (the only type of system we consider here) one has

$$\hat{U} = \sum_{i<j} U(r_i, r_j) = \sum_{i<j} \frac{q^2}{|r_i - r_j|} \quad (3)$$

Note that this is the same operator for any system of particles interacting via the Coulomb interaction, just as the kinetic energy operator

$$\hat{T} = -\frac{\hbar^2}{2m} \sum_i \nabla_i^2 \quad (4)$$

is the same for any nonrelativistic system.⁷⁷ whether our system is an atom, a molecule, or a solid thus depends only on the potential $v(r_i)$. For an atom, e.g.,

$$\hat{V} = \sum_i v(r_i) = \sum_i \frac{Qq}{|r_i - R|} \quad (5)$$

Where Q is the nuclear charge⁷⁸ and R the nuclear position. When dealing with a single atom, R is usually taken to be the zero of the coordinate system. For a molecule or a solid one has

$$\hat{V} = \sum_i v(r_i) = \sum_{ik} \frac{Q_k q}{|r_i - R_k|} \quad (6)$$

Where the sum on k extends over all nuclei in the system, each with charge $Q_k = Z_k e$ and position R_k . It is only the spatial arrangement of the R_k (together with the corresponding boundary conditions) that distinguishes, fundamentally, a molecule from a solid. Similarly, it is only through the term

\hat{U} that the (essentially simple) single-body quantum mechanics of Eq. (1) differs from the extremely complex many-body problem posed by Eq. (2). The key consequence of observation is that in order to calculate energy we can summarise the step as:-

$$\begin{aligned} \text{E is the energy of ground state} \quad n(r) &\xrightarrow{F} E & E = F[n(r)] \\ \text{E is the energy of an excited state} \quad \psi(r_1, r_2 \dots r_N) &\xrightarrow{F} E & E = F[\psi(r_1, r_2 \dots r_N)] \end{aligned} \quad (7)$$

i.e., one specifies the system by choosing $v(r)$, plugs it into Schrödinger's equation, solves that equation for the wave function Ψ , and then calculates observables by taking expectation values of operators with this wave function. One among the observables that are calculated in this way is the particle density

$$n(r) = N \int d^3r_2 \int d^3r_3 \dots \int d^3r_N \psi^*(r_1, r_2 \dots r_N) \psi(r_1, r_2 \dots r_N). \quad (8)$$

Many powerful methods for solving Schrödinger's equation have been developed during decades of struggling with the many-body problem. In physics, for example, one has diagrammatic perturbation theory (based on Feynman diagrams and Green's functions), while in chemistry one often uses configuration interaction (CI) methods, which are based on systematic expansion in Slater determinants. A host of more special techniques also exists. The problem with these methods is the great demand they place on one's computational resources: it is simply impossible to apply them efficiently to large and complex systems. Nobody has ever calculated the chemical properties of a 100-atom molecule with full CI, or the electronic structure of a real semiconductor using nothing but Green's functions.

It is here where DFT provides a viable alternative, less accurate perhaps, but much more versatile. DFT explicitly recognizes that nonrelativistic Coulomb systems differ only by their potential $v(\mathbf{r})$, and supplies a prescription for dealing with the universal operators \hat{T} and \hat{U} once and for all. Furthermore, DFT provides a way to systematically map the many body problem, with \hat{U} , onto a single-body problem, without \hat{U} . All this is done by promoting the particle density $n(\mathbf{r})$ from just one among many observables to the status of key variable, on which the calculation of all other observables can be based. This approach forms the basis of the large majority of electronic-structure calculations in physics and chemistry. Much of what we know about the electrical, magnetic, and structural properties of materials has been calculated using DFT, and the extent to which DFT has contributed to the science of molecules is reflected by the 1998 Nobel Prize in Chemistry, which was awarded to Walter Kohn, the founding father of DFT, and John Pople, who was instrumental in implementing DFT in computational chemistry.

The density-functional approach can be summarized by the sequence:

$$\boxed{n(\mathbf{r}) \Rightarrow \Psi(\mathbf{r}_1, \dots, \mathbf{r}_N) \Rightarrow v(\mathbf{r})} \quad (9)$$

i.e., awareness of $n(\mathbf{r})$ implies knowledge of the wave function and the potential, and hence of all other observables. Although this sequence describes the conceptual structure of DFT, it does not really represent what is done in actual applications of it, which typically proceed along rather different lines, and do not make explicit use of many-body wave functions. The following chapters attempt to explain both the conceptual structure and some of the many possible shapes and disguises under which this structure appears in applications.

3.1.1 Hohenberg Kohn theorem

The statement that the total energy of a many-electron system is a functional of the electron density goes under the name of the Hohenberg-Kohn theorem (Hohenberg and Kohn, 1964). Since the proof of this theorem is instructive and simple enough, we outline it here. The proof is based on the following three premises, which will be justified later:

- 1) In the ground state the electron density determines uniquely the external potential of the nuclei,
- 2) In any quantum state the external potential, determines uniquely the many electron wavefunction:
- 3) In any quantum state the total energy, E , is a functional of the many-body wavefunction by combining these premises we infer that, in the ground state, the density determines uniquely the total energy. This indicates that the total energy must be a functional of the density: $E = F[n]$.

This simply means that if we change the positions (or atomic species) of the nuclei we will obtain a different many-body wavefunction. This is intuitive and it does not require any proof. The first statement is not intuitive, but can be demonstrated by reduction and absurdum (Hohenberg and Kohn, 1964). The idea is to start from the assumption that the same ground-state electron density can be obtained from two different external potentials, and show that this leads to a contradiction.

In order to outline the proof it is helpful to introduce the following symbolic notation

For the kinetic energy and for the Coulomb energy:

$$\hat{T} = - \sum_i \frac{1}{2} \nabla_i^2, \quad \hat{W} = \frac{1}{2} \sum_{i \neq j} \frac{1}{|r_i - r_j|} \quad (10)$$

Using this notation the total energy.

$$E = \langle \psi | \sum_i V_n(r_i) | \psi \rangle + \langle \psi | \hat{T} + \hat{W} | \psi \rangle \quad (11)$$

By using the relation between the electron density and the wavefunction we discover that the first term can be rewritten in compact form using the electron density. We obtain:

$$E = \int dr n(r)V_n(r) + \langle \psi | \hat{T} + \hat{W} | \psi \rangle \quad (12)$$

3.1.2 Kohn-Sham equations

The Hohenberg-Kohn theorem tells us that the total energy of many electrons in their ground state is a functional of the electron density. However, this theorem does not say anything about how to construct such functional. While the exact form of this functional is still unknown, since the original work by Hohenberg and Kohn a number of very useful approximations have been developed.

$$F[n] = \int dr n(r)V_n(r) + \langle \psi[n] | \hat{T} + \hat{W} | \psi[n] \rangle \quad (13)$$

Here, we see that the first term in the functional is already explicitly dependent on the density, n ; however, there are two extra terms (kinetic energy and Coulomb energy) for which the dependence on the density is only implicit. The idea of Kohn and Sham (1965) was to split these implicit terms into the kinetic and Coulomb energy of independent electrons plus an extra term which accounts for the difference:

$$E = F[n]$$

Total energy in the independent electrons approximation

$$= \underbrace{\int dr n(r) V_n(r)}_{\text{External potential}} - \underbrace{\sum_i \int dr \phi_i^*(r) \frac{\nabla^2}{2} \phi_i(r)}_{\text{Kinetic energy}} + \underbrace{\frac{1}{2} \int \int dr dr' \frac{n(r)n(r')}{|r - r'|}}_{\text{Hartree energy}} + \underbrace{E_{xc}[n]}_{\text{XC energy}} \quad (14)$$

The free electron gas is the simplest model of electrons in a solid. In this model, it is assumed that electrons do not interact with each other, that the potential due to the nuclei is simply a constant (which can be set to zero for convenience) and that the N electrons are contained in a large box of volume V . Under these assumptions the eigenstates and eigenvalues in Hartree units are given by (Kittel, 1976):

$$\phi_k(r) = \frac{1}{\sqrt{V}} \exp(iK \cdot r) \text{ and } \epsilon_k = \frac{|k|^2}{2}. \quad (15)$$

These solutions represent stationary waves with wavevectors k . The eigenvalue of the highest occupied state is the Fermi energy, ϵ_F , and the corresponding wavevector is the Fermi wavevector, k_F , so that $\epsilon_F = k_F^2/2$.

The beauty of the free electron gas model is that all its physical properties depend on one single parameter, the electron density, $n = N/V$. For example, the Fermi wavevector is related to the density by:

$$k_F = (3\pi^2 n)^{\frac{1}{3}} \quad (16)$$

The availability of a practical approximation for the exchange and correlation energy, as given by the LDA, allows us to obtain the final ingredient needed for solving the Kohn-Sham equations, namely the exchange and correlation potential. In fact, given the LDA exchange and correlation energy, $E_{xc}[n]$; we can obtain V_{xc} by using the functional derivative.

The result of this functional derivative for the exchange interaction has the following very simple expression:

$$V_x(r) = - \left(\frac{3}{\pi}\right)^{\frac{1}{3}} n^{\frac{1}{3}}(r). \quad (17)$$

This expression is very appealing because, in order to obtain the exchange potential at point r , we need to know only the density at the same point, $n(r)$. The expression for the correlation potential is slightly more complicated but also in that case only the local density is needed; i.e. the correlation potential at a given point is determined by the density at the same point.

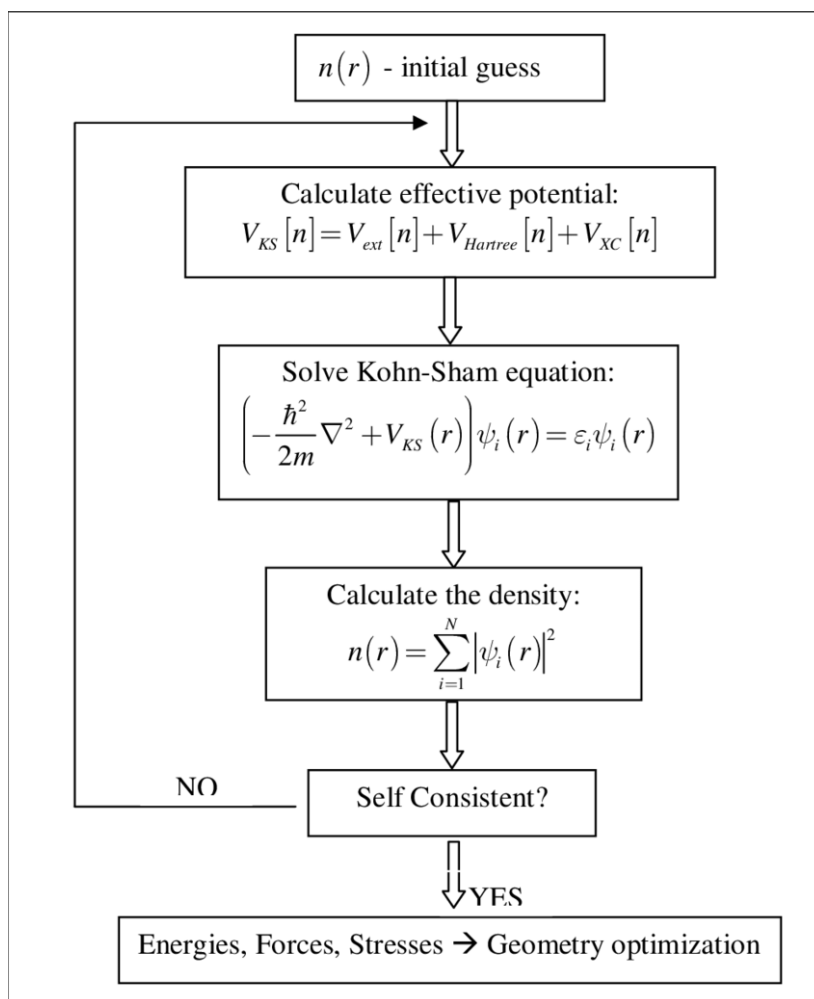


Figure 10: Schematic flowchart for finding self-consistent solutions to Kohn-Sham equations.

Numerical algorithms for solving the Kohn-Sham equations are currently implemented in a large number of software packages, many of which are freely available online. These packages allow one to comfortably execute calculations on molecules and crystals with small unit cells even on personal computers. However, most of these packages are designed and optimized in order to be executed on large parallel computers, ranging from small research clusters (of the order of 100 processors) to national high-performance computing facilities (of the order of 100,000 processors). Today the combination of DFT with high-performance computing provides us with a very powerful tool for understanding and predicting material properties starting from the first principles of quantum mechanics.

Despite the success and widespread use of DFT, it is important to bear in mind that it addresses the electronic ground state of materials. Stated otherwise, DFT is not designed to describe electronic excitations and non-equilibrium phenomena. For example, the Kohn-Sham formulation of DFT is able

to predict accurately the equilibrium structures of semiconductors, but it cannot be used for predicting with quantitative accuracy their corresponding optical properties.

A non-exhaustive list of material properties which can be calculated with good accuracy using DFT would include:

- equilibrium structures,
- vibrational properties and vibrational spectra,
- binding energies of molecules and cohesive energies of solids,
- ionization potential and electron affinity of molecules,
- electronic band structures and total density of states i.e. electronic properties of metals and semiconductors.

On the other hand, material properties which cannot be calculated reliably using DFT include:

- electronic band gaps of semiconductors and insulators,
- magnetic properties of Mott{Hubbard insulators (mostly systems with atomic-like localized d or f electronic states)
- Bonding and structure in sparse matter, e.g. proteins, where van der Waals forces are important.

From this list it should be clear that DFT has a number of limitations and cannot be expected to be a ‘universal’ tool for calculating material properties.

3.2 Computational study of material

Equilibrium crystal structures, optimized geometries, and electronic properties of the CsPbBr₃ perovskite material i.e., band structure and density of states (DOSs) were calculated by hybrid periodic density functionals theory (DFT)⁷⁹⁻⁸² method including Grimme’s dispersion corrections noted by B3LYP-D3^{83,84} method implemented in *ab initio* CRYSTAL17 suite code.⁸⁵⁻⁸⁷ The electronic properties calculations were obtained by using the same B3LYP-D3 method.⁸⁸⁻⁹⁴ CRYSTAL17 makes use of localized (Gaussian type) basis sets^{95,96}. Grimme’s semi-empirical third-order dispersion correction parameters (Grimme’s-D3)⁹⁷ were added in the DFT computation to incorporate weak van der Waals interaction.⁹⁸ Triple-zeta valence with polarization quality pob_TZVP_rev2 basis sets were used for

Bromine (Br)⁹⁹ and for Caesium (Cs)¹⁰⁰ Cs HAYWSC-31(2df) type basis sets and for Lead (Pb)¹⁰¹ ECP60MDF-6111(51d) G. A set of (8x8x8) Monkhorst-Pack k-point grids was carried out for geometric optimization.^{102,103} the atomic orbitals of Cs, Pb and Br atoms were used to compute and plot the total DOSs. These k-points are used for the integration inside the first Brillouin zone. VESTA,¹⁰⁴ a visualization code, was used to create the graphics and analysis of the crystal structure of all the systems. The convergence threshold was set at 10^{-7} a.u. to evaluate the convergence of the energy, forces, and electron density.

From the 3D Crystal structure CsPbBr₃. We cleaved a surface from it and computational developed the 2D vacuum slab. The periodic structure computation and the equilibrium structures were optimized by performing hybrid dispersion corrected density functional theory (DFT) (here B3LYP-D3 method) using CRYSTAL17 suite code. The electronic properties calculations i.e., band structures and density of states (DOSs) were obtained by using the same B3LYP-D3 method.¹⁰⁵ In the calculation, we have accounted for the weak long-range van der Waals effects resulting from the interaction between atoms by including third order dispersion in DFT computation. CRYSTAL 17 code uses Gaussian type basis set¹⁰⁶. To account for the Gaussian type of atomic orbitals of the atoms, Triple-zeta valence with polarization quality (TZVP)¹⁰⁷ Gaussian type basis sets were used for O atoms, the relativistic effective core potentials HAYWSC-31(2df) and ECP60MDF-6111(51d)G were used for Cs and Pb atoms in the present calculations. All the integrations of the first Brillouin zone were sampled for CsPbBr₃ (20x20x1) Monkhorst-Pack used.

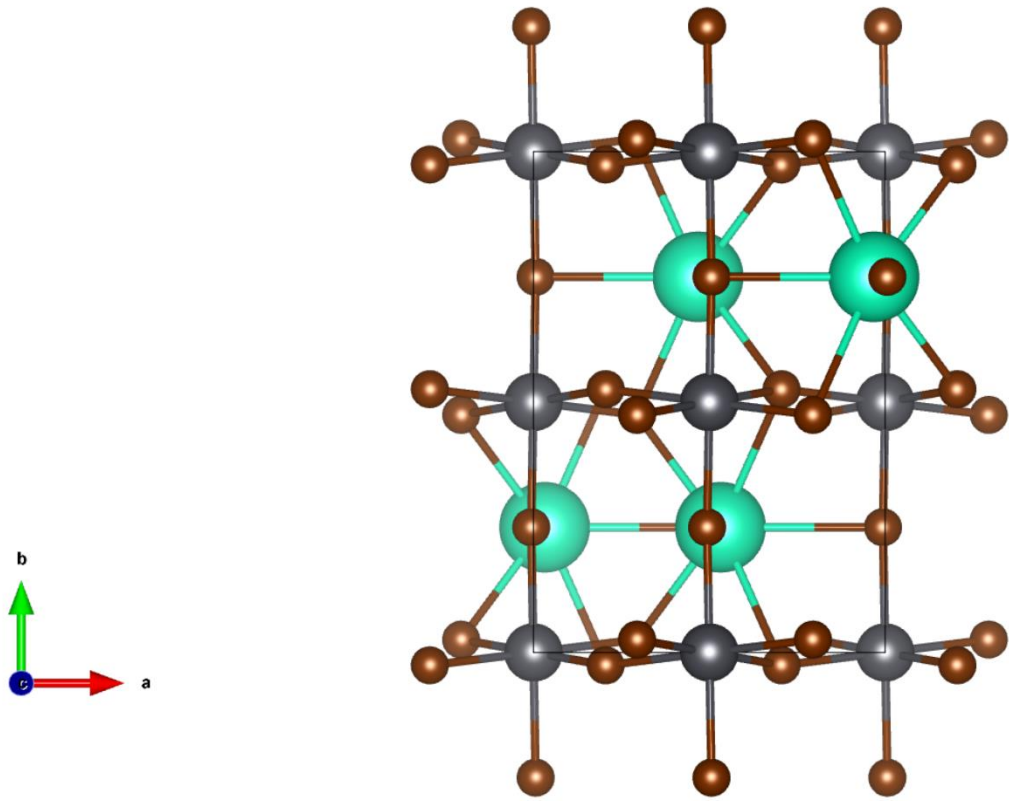


Figure 11: The equilibrium structure of the unit cell CsPbBr_3 computed by B3LYP-D3 method.

Table 2: The equilibrium lattice parameters of 3D Crystal of CsPbBr_3 .

Material	CsPbBr_3
Lattice constants ($a=b$)	$a= 8.18 \text{ \AA}$ $b= 11.92 \text{ \AA}$
Adjacent angles (α, β and γ)	90.0°
Space group symmetry	PNMA
Average bond distance	Cs – Br 3.749 Br - Pb 2.973

Chapter 4

4 Results and discussions

We have performed a theoretical and computational study on the 3D CsPbBr₃ perovskite-type of material to obtain the equilibrium geometry and electronic properties of the same. The DFT-D study showed that CsPbBr₃ material has *Pnma* space-group symmetry. The equilibrium lattice constant of the optimized CsPbBr₃ are found to be $a = 8.186 \text{ \AA}$, $b = 11.929 \text{ \AA}$, $c = 8.108 \text{ \AA}$ and $\alpha = \beta = \gamma = 90.0^\circ$. The equilibrium bond distance of Cs - Br and Br - Pb was found to be 3.749 \AA and 2.973 \AA computed by the DFT-D method and the optimized geometry of the 3D CsPbBr₃ is given in Fig 12 (a). For the band structure and density of states calculations, we selected the *k*-vector path from $\Gamma - Z - Y - X - S - U - \Gamma$ for the materials. Computationally, we obtained the band gap is at 3.9 eV. The atomic orbitals of Cs, Pb, and Br were used to compute and plot the total density of states (DOSs). The band structure and density of states calculation has been done for the normalized wave function which can be seen from Fig 12 (b) and Fig12 (c).

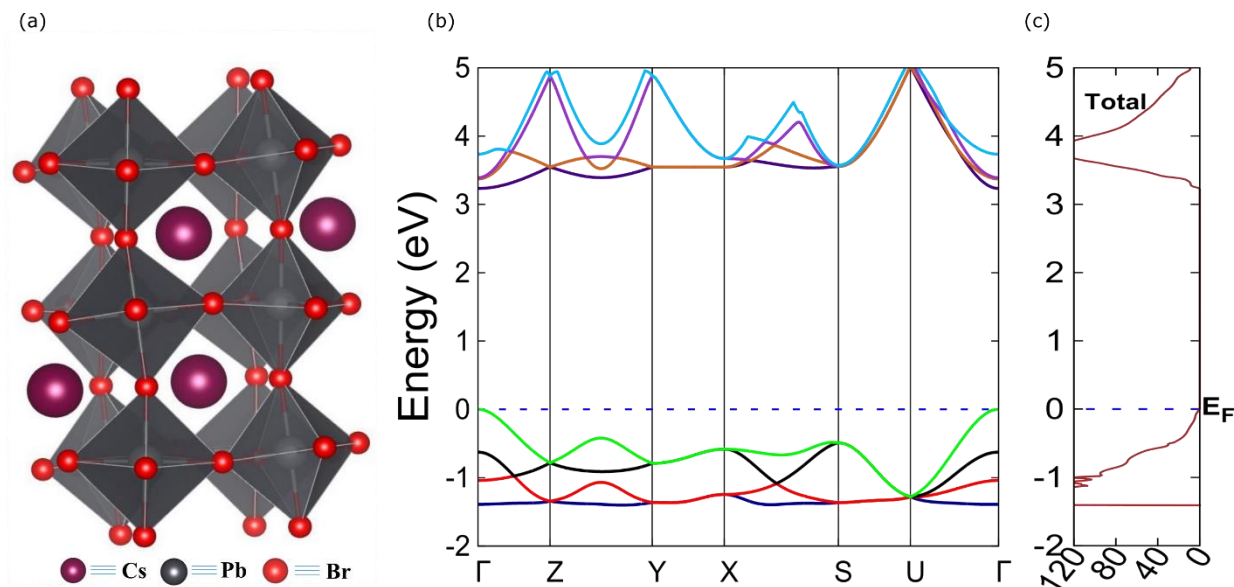


Figure 12: Equilibrium 3D crystal structure of the CsPbBr₃ perovskite with band structure and density of states.

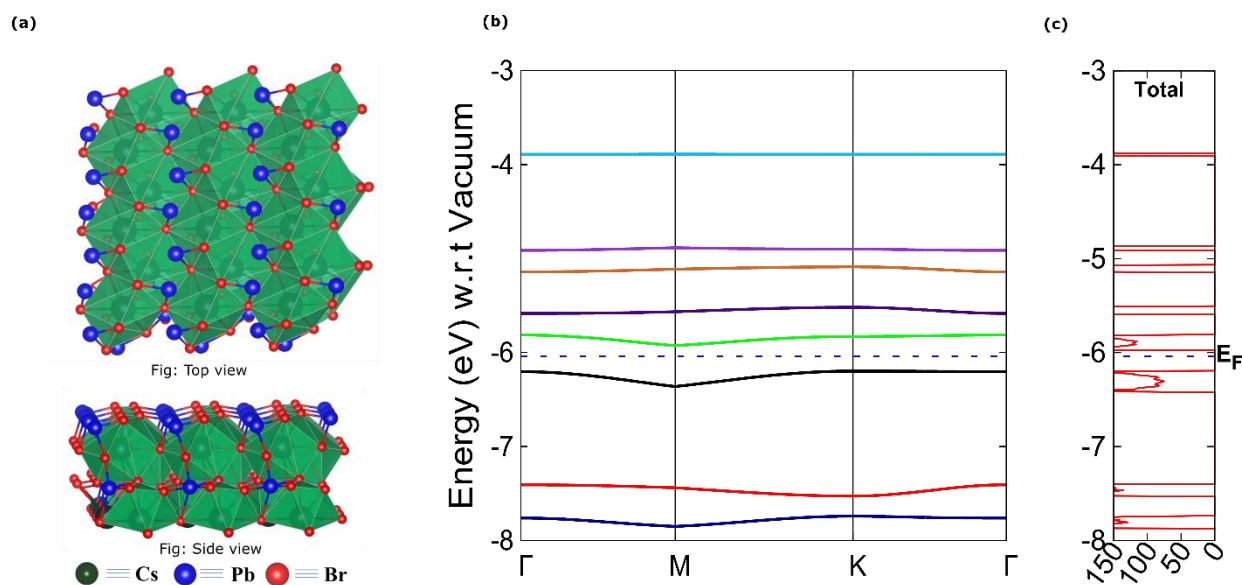


Figure 13: Equilibrium 2D monolayer structure of CsPbBr₃ (top view) and (side view) perovskite with band structure and density of states.

After the optimization and electronic property calculation from the band plot. We observe our CsPbBr₃ 3D perovskite material has a high band gap about 3.9 eV. Because of this large amount of band gap it is an insulator, so it cannot work as an electrocatalyst for ORR application. We have cleaved a

surface (0 0 1) from the 3D crystal structure of the CsPbBr₃. We computationally developed the 2D monolayer structure of the perovskite with 500 Å vacuum space in z-direction, i.e. there is no symmetry along the z-axis, and we performed the equilibrium structure calculation and electronic properties of the 2D layer material of the CsPbBr₃. After optimization, the equilibrium lattice constants were found to be $a = 11.929 \text{ \AA}$, $b = 8.186 \text{ \AA}$ and $\alpha = \beta = \gamma = 90^\circ$. We have plotted the band structure and density of states and we found that the band gap is 0.22 eV. Also the similar properties calculations were performed for the reaction intermediates occurring in the ORR. Its band gap values have been listed in Table below.

Table 3: The equilibrium lattice parameters of 3D Crystal and 2D monolayer of CsPbBr₃.

System	Lattice constant (a, b, c in Å)	Angle (α, β, γ in Degree)	Space Group symmetry	Bond Type	Distance in Å
CsPbBr ₃	a= 8.186 Å	$\alpha = \beta = \gamma = 90.0$	<i>Pnma</i>	Cs – Br	3.749
	b= 11.929 Å			Br - Pb	2.973
2D Monolayer CsPbBr ₃	a= 11.929 Å	$\alpha = \beta = \gamma = 90.0$	<i>P1</i>	Cs – Br	3.757
	b= 8.186 Å			Br - Pb	2.967

4.1 REACTION PATHWAY:

The following reaction pathway has been proposed for the ORR (as shown in Figure 15). At first, the pure 2D CsPbBr₃ was prepared as most reaction takes place on the surface. Then, O₂ from the solvent comes and gets attached to the Pb site. Thereafter that O₂ gets split and one oxygen atom from the O₂ goes on to the Br site. Then one proton and one electron attack the structure and OH is formed at the Br site and then H₂O gets removed and then again H⁺ and electron combines with structure to give OH at the Pb site and thereafter goes on to being CsPbBr₃ by removal of H₂O. This reaction mechanism has been schematically represented in Figure 15 with the reaction intermediates occurring during ORR. The 2D layered structure, Band structure and DOSS of the various reaction intermediates has been illustrated in figure 17, 18, 19, 20, and 21 respectively.

After electronic structure properties calculation we were ready to investigate the 2D slab for catalytic performance in ORR. The reaction pathway scheme by depicting all the major reaction intermediates has been illustrated in Figure 14 and the overview of each step is shown in figure 15.

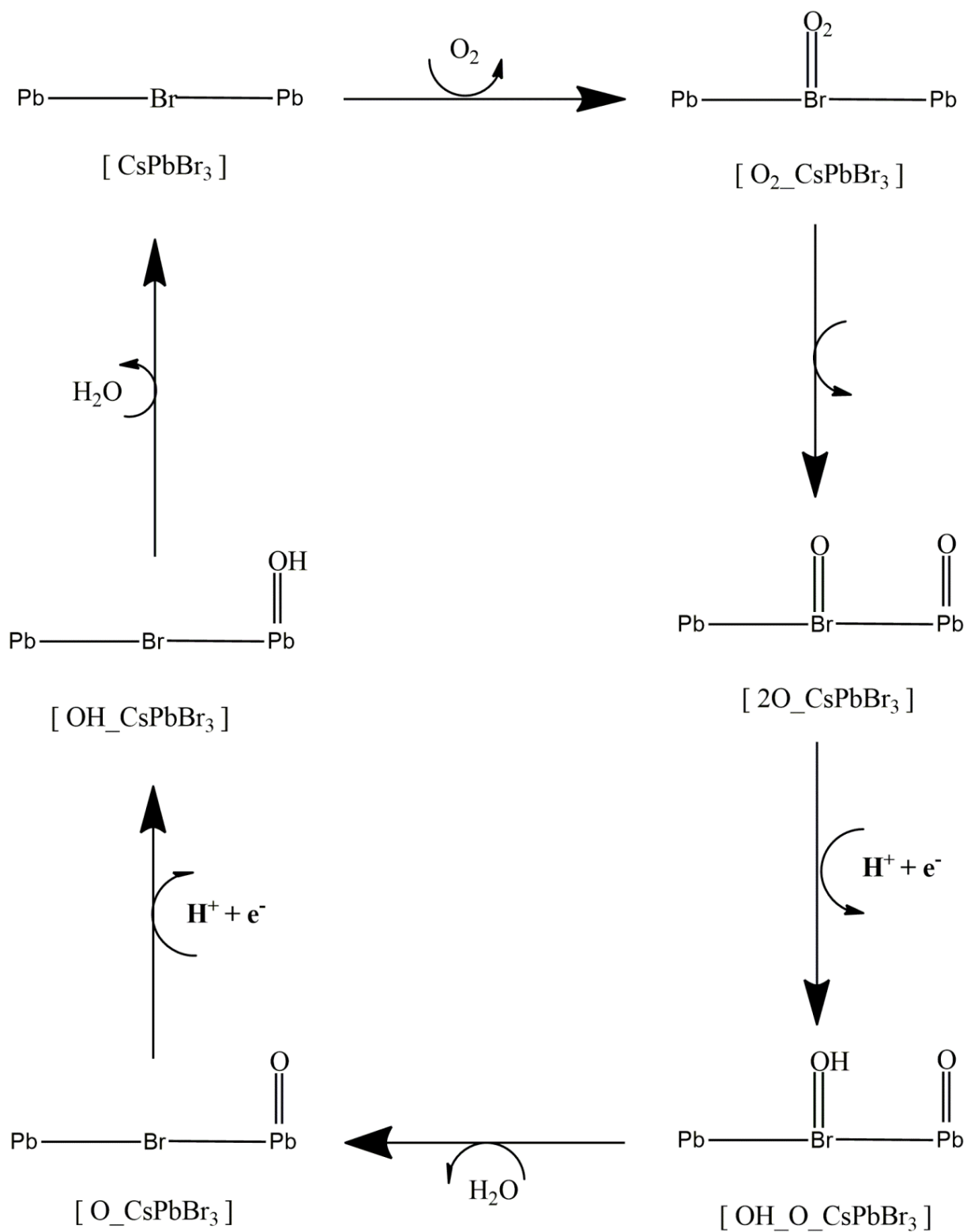


Figure 14: Reaction pathway scheme for ORR.

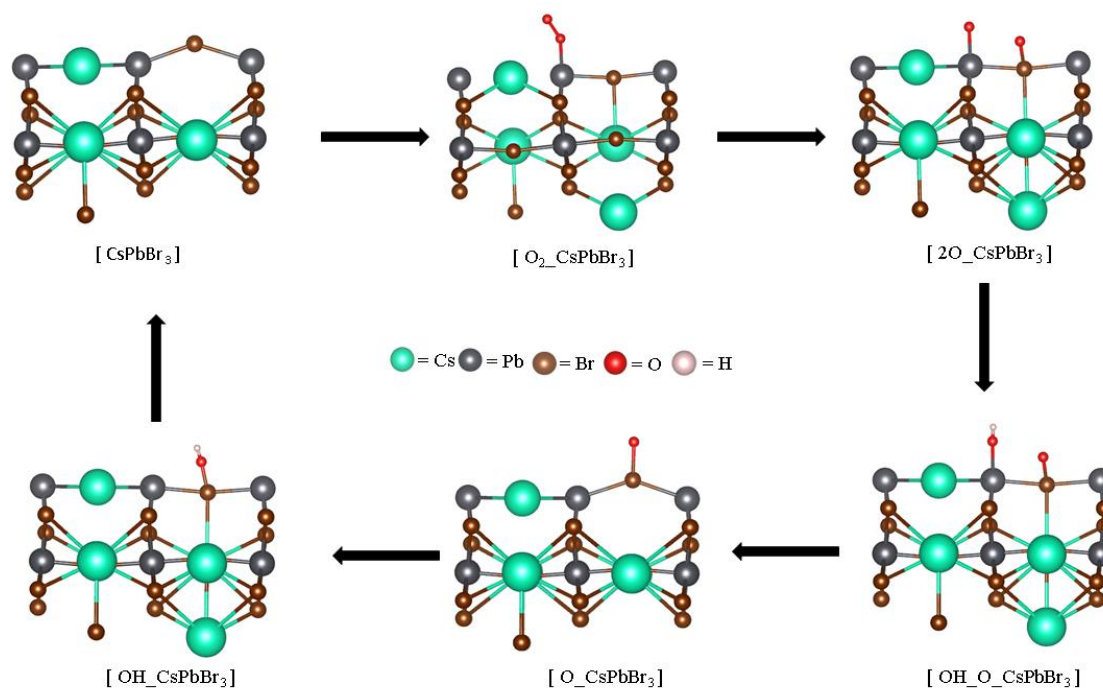


Figure 15: Proposed Reaction pathway scheme for ORR on the surface of the 2D CsPbBr₃.

The proposed oxygen reduction reaction shown in the diagram (Figure 15) is a four-electron route or four electron transfer mechanism i.e., $O_2 + 4H^+ + 4e^- \rightarrow 2H_2O$. The adsorption behaviour at the active site of the catalyst is believed to be the key parameter in the efficient ORR. We started off with the computational modelling of the gas phase reaction steps. At standard hydrogen electrode condition i.e., when pH=0, the first step is the oxygen molecule (O_2^*) is adsorbed on the Pb site of the layered perovskite. The bond length of Pb-O bond was found to be 2.3 Å. The energy change during this step was calculated to be -6.20 eV. Now the adsorbed O_2^* dissociates into $2O^*$ with one of the oxygen atom getting adsorbed to Br site. Here the Pb-O bond was still 2.3 Å and the Br-O distance was observed to be 1.78 Å. Thereafter, there is addition of a proton and an electron and the Br-O bond length changes from 1.78 Å to 1.77 Å and the energy change was calculated to be -6.72 eV. Furthermore, one proton

and an electron is attached to the OH* site and then there is removal of H₂O from the surface of the catalyst. The equilibrium lattice parameters at each reaction intermediate is listed in Table 4.

Table 4: The equilibrium lattice parameters of various steps of ORR has been tabulated here.

System	Lattice Constants (a, b, c in Å)	Angle (α, β, γ in Degree)	Space Group Symmetry	Band gap (eV)	Distance in Å				
					Cs-Br H	Pb-Br	Br-O	Pb-O	O-H
O₂_CsPbBr₃	a= 11.689 b= 7.390	$\alpha = \beta = \gamma =$ 90.00	<i>P I</i>	1.89	3.71	2.97	----	2.30	----
2O_CsPbBr₃	a= 11.900 b= 7.660	$\alpha = \beta =$ 90.00 $\gamma = 89.80$	<i>P I</i>	0.22	3.71	2.97	1.78	2.30	----
OH_O_CsPbBr₃	a= 11.814 b= 7.366	$\alpha = \beta = \gamma =$ 90.00	<i>P I</i>	3.58	3.71	2.97	1.77	2.30	0.93
O_CsPbBr₃	a= 12.176 b= 8.700	$\alpha = \beta =$ 90.00 $\gamma = 89.17$	<i>P I</i>	0.15	3.71	2.97	2.07	----	----
OH_CsPbBr₃	a= 11.843 b= 8.130	$\alpha = \beta = \gamma =$ 90.00	<i>P I</i>	0.50	3.71	2.97	1.69	----	0.88

B3LYP-D3 calculation has been performed to obtain the optimized structures for different reaction steps involved in the ORR process and the details of the optimized structures after all the atoms of the respective systems acquire their minimum energy positions, including their lattice constants, angle between the lattice vectors, symmetry of different reaction steps, their respective band gaps and the bond length of newly formed bonds at the successive steps are presented in an integral form in the above table.

The similar process as mentioned above is repeated again and again and from the energy calculations it is clear that [OH_O_CsPbBr₃] → [O_CsPbBr₃] is the rate determining step in the ORR mechanism. The energy changes happening at each stage of the reaction is listed in Table 5.

Table 5: Change in free energy ΔG (eV) of all reaction steps intermediates of oxygen reduction reaction (ORR) performed on our material CsPbBr₃.

ORR Steps	ΔG (eV)
[CsPbBr ₃] → [CsPbBr ₃ _O ₂]	-6.20
[CsPbBr ₃ _O ₂] → [CsPbBr ₃ _2O]	1.38
[CsPbBr ₃ _2O] → [OH_O_CsPbBr ₃]	-6.72
[OH_O_CsPbBr ₃] → [O_CsPbBr ₃]	-5.88
[O_CsPbBr ₃] → [OH_CsPbBr ₃]	-17.34
[OH_CsPbBr ₃] → [CsPbBr ₃]	-12.16

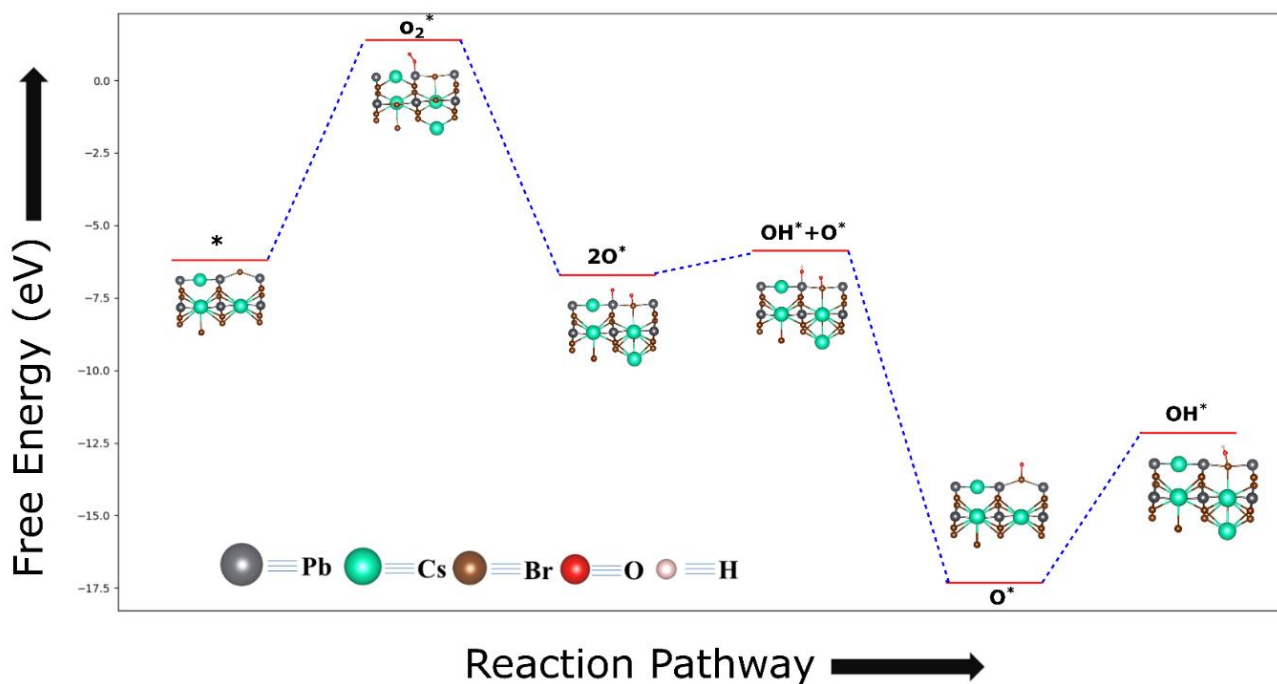


Figure 16: Free energy calculation diagram for ORR pathway on CsPbBr₃.

All the optimised structures, band and DOSS calculations for each reaction intermediate is shown in Figure 17, 18, 19, 20 and 21.

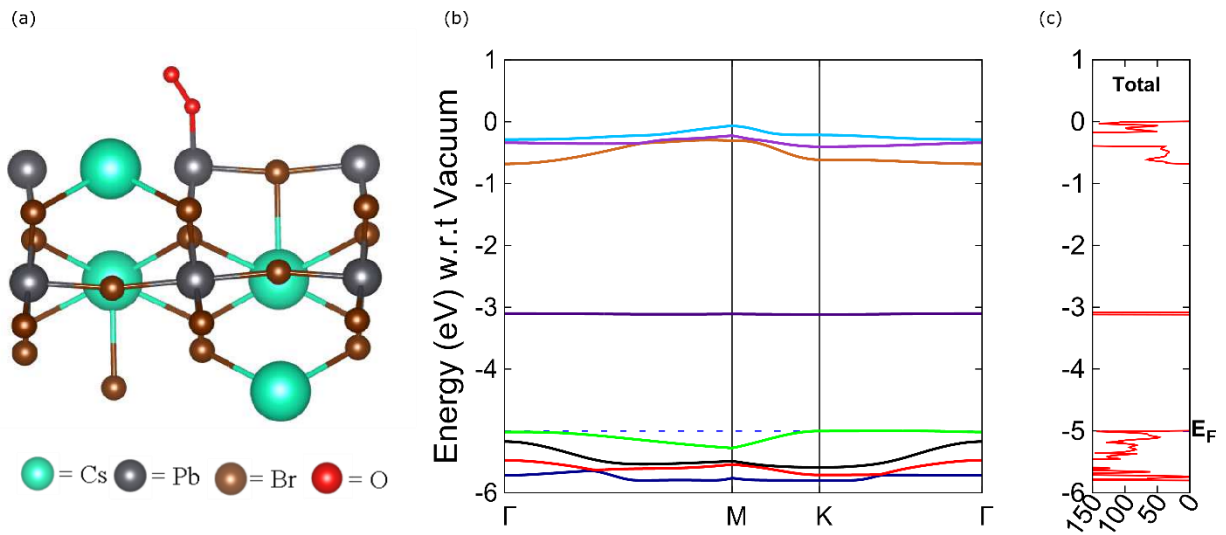


Figure 17: A 2D monolayer structure of $O_2\text{-CsPbBr}_3$ with band structure and density of states.

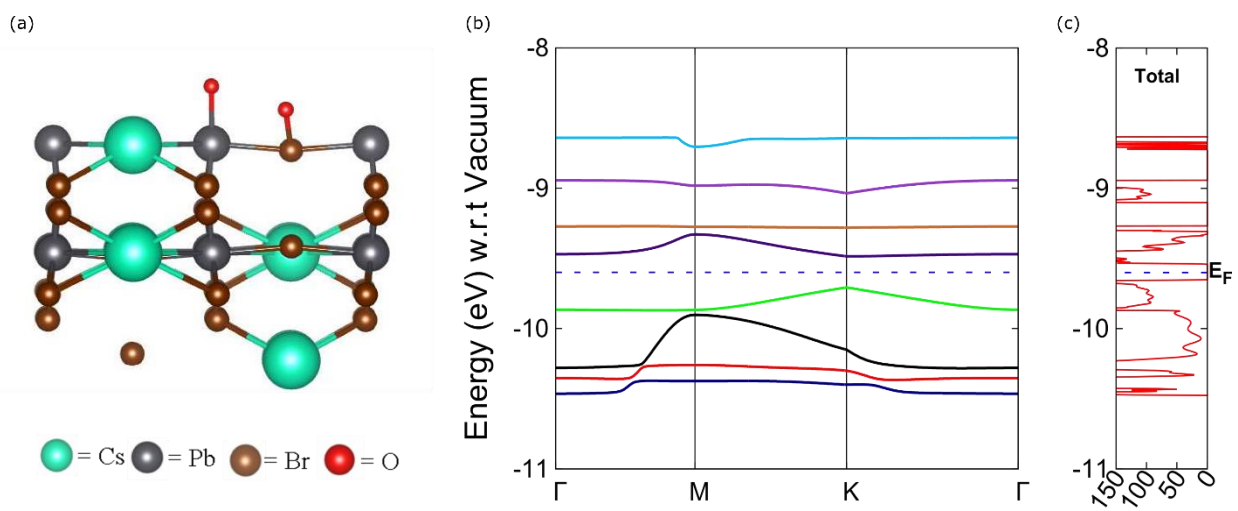


Figure 18: A 2D monolayer structure of $2O\text{-CsPbBr}_3$ with band structure and density of states.

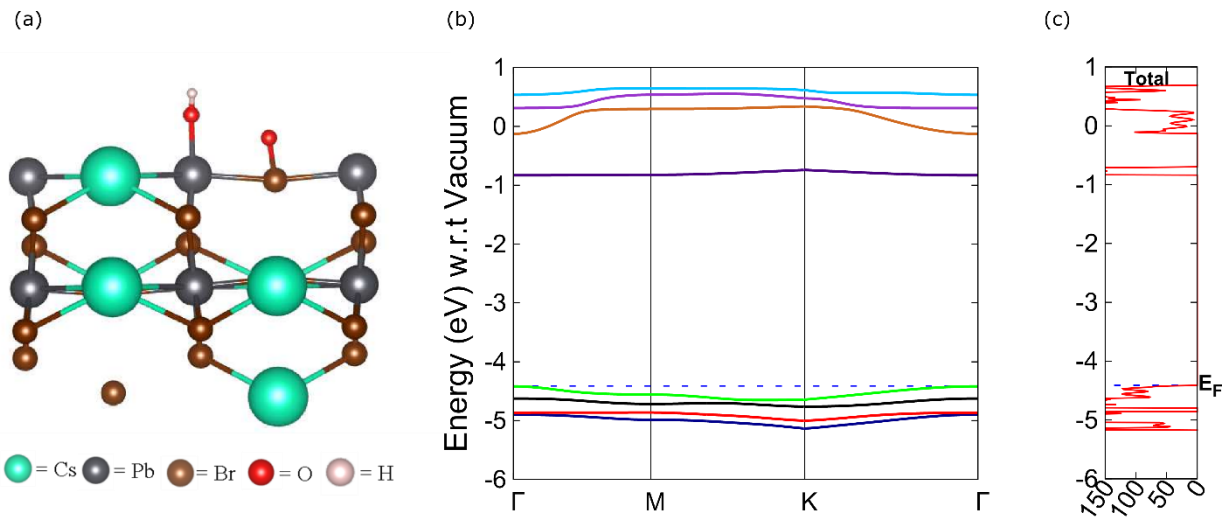


Figure 19: A 2D monolayer structure of OH_O-CsPbBr₃ with band structure and density of states.

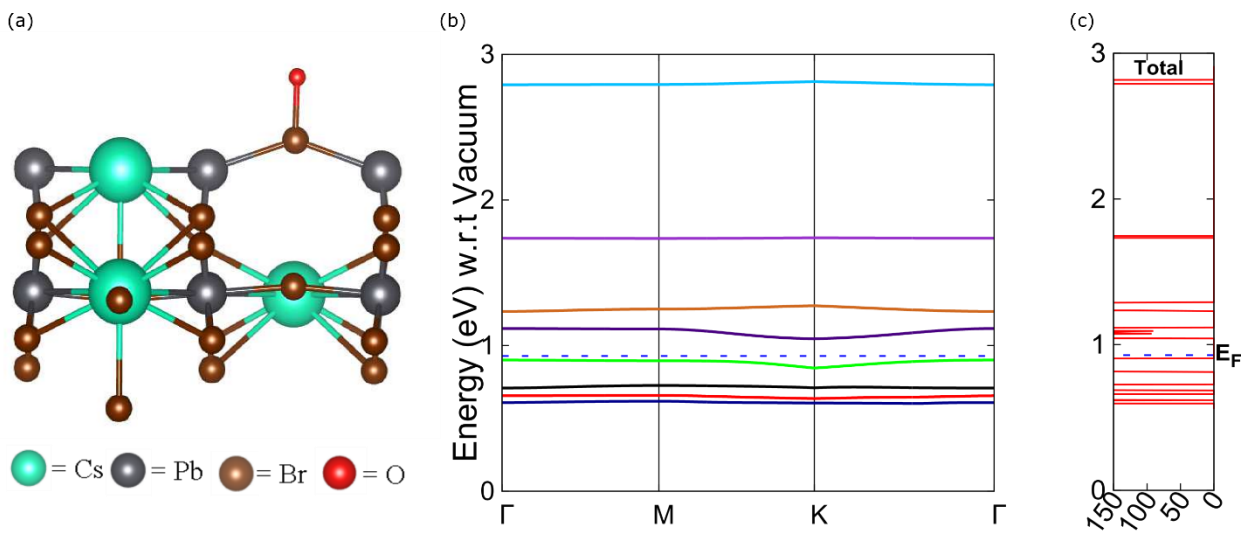


Figure 20: A 2D monolayer structure of O-CsPbBr₃ with band structure and density of states.

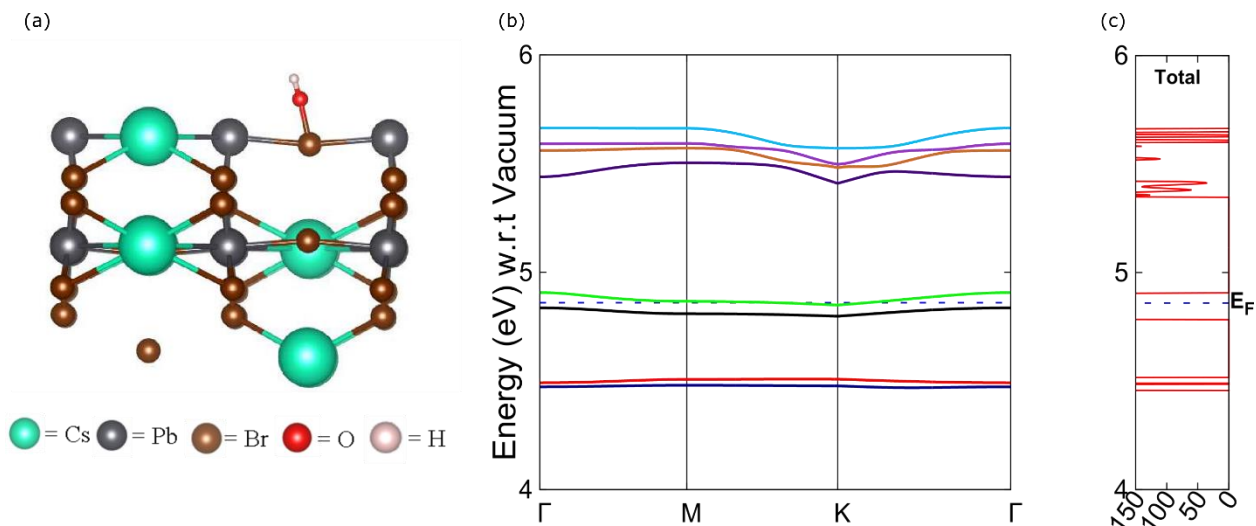


Figure 21: A 2D monolayer structure of OH_CsPbBr₃ with band structure and density of states.

DFT-D3 methodology was used to obtain the optimized structure for the CsPbBr₃ with an O₂ attached to the Pb edge site (O₂_CsPbBr₃) of the pristine CsPbBr₃. The optimized structure formed computationally after the oxygen molecule attached to the Pb's site is illustrated in Fig 17(a). This study shows that after all the atoms of O₂_CsPbBr₃, acquire their minimum energy position, the bond length between different atoms of O₂_CsPbBr₃ is elaborated in the above Table 5. We found that the compound has the P1 symmetry with the lattice constant $a = 11.689 \text{ \AA}$, $b = 7.390 \text{ \AA}$, and the angle between a and b i.e., $\gamma = 90.00^\circ$. The figures 17(b) and 17(c) shows the DFT-D computational calculations of energy band structure and total density of states of the compound, respectively. The former Fig 17(b) has drawn for a symmetric direction of the crystal momentum vector $\Gamma - M - K - \Gamma$ with respect to the vacuum, and it shows that the computationally the Fermi energy (E_F) level was obtained at $E_F = -5.00 \text{ eV}$. From the Figure 17(b), it also can be confirmed that the lowest of the conduction band was found at -3.1 eV and the highest of the valence band was obtained at -4.9 eV both at K point which ensure that the compound O₂_CsPbBr₃ has a direct band gap of 1.89 eV at K point. Now, we can say that the compound is semiconductor in nature. The later Fig 17(c), density state calculation of the compound O₂_CsPbBr₃ shows that there is an electron density around the Fermi level. The most contribution towards the density of states of compound is from its metallic part.

The Figure 18(a) shows the optimized 2D monolayer structure of 2O_CsPbBr₃ in which one oxygen atom from the oxygen molecule of the Pb site is migrated to the Br site. The DFT-D calculation found its lattice constant values as $a = 11.900 \text{ \AA}$, $b = 7.660 \text{ \AA}$ and $\gamma = 89.00^\circ$ with P1 symmetry with a formation

of new bond Br-O at the Br site which is a transition state with positive Gibbs free energy change during the reaction step $\text{CsPbBr}_3\text{-O}_2$ to 2O-CsPbBr_3 . Similarly, Figures 18(b) and 18(c) show the DFT-D calculations of energy band structure and total density of state of the so formed compound, respectively. In fig 18(b) the energy band diagram is plotted for the crystal momentum vector in a symmetric direction $\Gamma - M - K - \Gamma$ with respect to the vacuum in this case the Fermi level was found to go further below towards the negative axis with a value of $E_F = -9.7$ eV. Again, the bottom of the conduction band and top of the valence band was found to move towards the Fermi energy level and separated by an energy band gap of 0.22 eV K-point. From the density of states calculation as depicted in the Figure 18(c) shows that there are occupancies of electrons below and up to the Fermi energy level, however there is no electron density is so available at the Fermi level in the both the lower and upper portion of the fermi energy level, the density of electrons is found to be more than in the case of $\text{CsPbBr}_3\text{-O}_2$.

In the similar way, Figure 19(a) illustrates the optimized 2D monolayer structure of OH-O-CsPbBr_3 in which one oxygen atom is bonded to the Pb site and the other oxygen atom is bonded with the Br site. The valence electron of the oxygen atom connected to the Pb site gets its inert configuration by bonding with hydrogen atom, forming an O-H bond with a minimized bond length of 0.93 Å. In the energy band diagram of Figure 19(b) tells that with the bonding of hydrogen with the oxygen atom the band energy of OH-O-CsPbBr_3 further increases and becomes 3.58 eV. This may be due to the bonding of valence electron of with the hydrogen which reduces the number of valence electrons available with the OH-O compound. In this case, the top of the valence band is crossed over the fermi energy level in the bottom of the conduction band is around 3.6 eV far from it. Figure 19(c) corresponding the density of state of the compound OH-O-CsPbBr_3 confirms the same. In this case, there is electron density found at the Fermi level.

In Figure 20(a), the oxygen atom so connected with to the Pb site has been reduced in the form of OH^- living behind an oxygen atom bonded to the Br site with a valence electron left. Creating a bond length of 2.07 Å in between the atom's Br and O. Due to the presence of valence electron of the oxygen atom the energy band gap at further reduces to 0.15 eV the same can be insured from the Figure 20(b). In this case the top of the valence band is much closer to the Fermi level then the bottom of the conduction band. The density of states (DOS) in Figure 20(c) also gives a total electron density much closer near to the Fermi level.

In Figure 21(a) the oxygen atom connected to the Br site has been bonded with a hydrogen atom resulting an O-H bond with a bond length of 0.88 Å. Due to this bonding between hydrogen and oxygen, the valence electron of the oxygen atom reduces so as the compound OH_CsPbBr₃ because of the decrease in the valence electron of the compound due to the bonding of oxygen atom, the energy band gap further increases 0.50 eV. And same can be seen in figure 21(b), for energy band of OH_CsPbBr₃ the top of the valence band is over crossed to the fermi level situated at $E_f = 4.9$ eV. From Figure 21(c), due to the crossing of top of the valence band over the Fermi level, there is an electron density at the fermi level and the same can be observed from Figure 21(c).

It is to be noted that the energy density in the DOS calculation is purely due to the valence bands at the same time the conduction bands are far apart from the fermi level. This DOS calculation Figure 21(c) shows that there is an occupancies at the Fermi level for the system OH_CsPbBr₃.

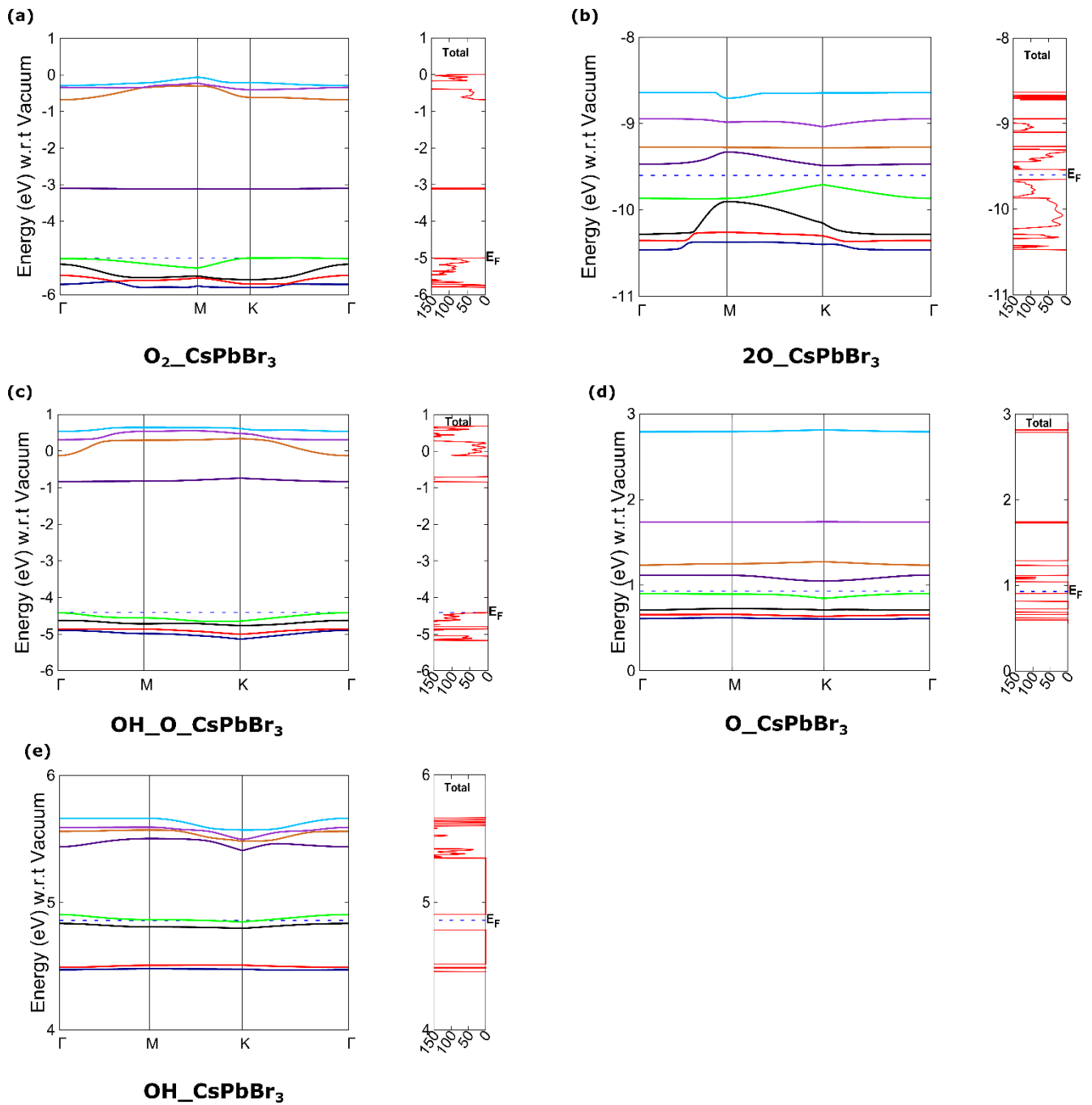


Figure 22: Band structure plot and density of states of each intermediate in the reaction pathway.

4.2 Conclusion:

We computationally developed 3D CsPbBr_3 and explored its electronic structure and properties. The study showed it as a semiconducting material. The band gap of 3D CsPbBr_3 material was high (3.9

eV) so obviously it would not be a very useful electrocatalyst. As most of the electrocatalytic reactions take place on the surface of the electrode so we made a vacuum slab of the material. And the present investigation found that it showed relatively lower band gap (0.5 eV) and then we relied on this 2D slab of the perovskite as a stepping stone for better electrocatalytic performance. So, the theoretical and computational study of the kinetics of ORR have been carried out by geometry optimisation of each important reaction intermediate in ORR. After optimisation, we performed energy calculations of the entire pathway and the values obtained from these calculations present that the 2D CsPbBr₃ shows excellent catalytic performance towards ORR. In summary, the computationally developed 2D CsPbBr₃ can be a promising catalytic material used in the electrode of fuel cells to efficiently carry out ORR with crucial improvement in the reaction kinetics.

References:

- 1 V. Bansal, P. Poddar, A. Ahmad and M. Sastry, *J. Am. Chem. Soc.*, 2006, **128**, 11958–11963.
- 2 D. Goldberg, I. N. McCave, J. H. Steele, S. Jin, T. H. Tiefel, M. McCormack, R. A. Fastnacht, R. Ramesh, L. H. Chen, K. Polytechnique Institute and T.-H. Hsiang, *R. H. Kra~chnan, Phys. Fluids*, 1971, **28**, 189–220.
- 3 J. G. Bednorz, M. Takashige and K. A. Müller, *Prop. Perovskites Other Oxides*, 2010, **193**, 555–565.
- 4 Y. Zhou and K. Zhu, *ACS Energy Lett.*, 2016, **1**, 64–67.
- 5 Z. K. Tan, R. S. Moghaddam, M. L. Lai, P. Docampo, R. Higler, F. Deschler, M. Price, A. Sadhanala, L. M. Pazos, D. Credgington, F. Hanusch, T. Bein, H. J. Snaith and R. H. Friend, *Nat. Nanotechnol.*, 2014, **9**, 687–692.
- 6 G. Li, Z. K. Tan, D. Di, M. L. Lai, L. Jiang, J. H. W. Lim, R. H. Friend and N. C. Greenham, *Nano Lett.*, 2015, **15**, 2640–2644.
- 7 Y. H. Kim, H. Cho, J. H. Heo, T. S. Kim, N. S. Myoung, C. L. Lee, S. H. Im and T. W. Lee, *Adv. Mater.*, 2015, **27**, 1248–1254.

- 8 X. Zhang, H. Lin, H. Huang, C. Reckmeier, Y. Zhang, W. C. H. Choy and A. L. Rogach, *Nano Lett.*, 2016, **16**, 1415–1420.
- 9 B. R. Sutherland and E. H. Sargent, *Nat. Photonics*, 2016, **10**, 295–302.
- 10 H. L. Zhu, J. Cheng, D. Zhang, C. Liang, C. J. Reckmeier, H. Huang, A. L. Rogach and W. C. H. Choy, *ACS Nano*, 2016, **10**, 6808–6815.
- 11 G. Xing, N. Mathews, S. S. Lim, N. Yantara, X. Liu, D. Sabba, M. Grätzel, S. Mhaisalkar and T. C. Sum, *Nat. Mater.*, 2014, **13**, 476–480.
- 12 H. Zhu, Y. Fu, F. Meng, X. Wu, Z. Gong, Q. Ding, M. V. Gustafsson, M. T. Trinh, S. Jin and X. Y. Zhu, *Nat. Mater.*, 2015, **14**, 636–642.
- 13 J. Xing, X. F. Liu, Q. Zhang, S. T. Ha, Y. W. Yuan, C. Shen, T. C. Sum and Q. Xiong, *Nano Lett.*, 2015, **15**, 4571–4577.
- 14 Y. Xu, Q. Chen, C. Zhang, R. Wang, H. Wu, X. Zhang, G. Xing, W. W. Yu, X. Wang, Y. Zhang and M. Xiao, *J. Am. Chem. Soc.*, 2016, **138**, 3761–3768.
- 15 D. Yang and D. Huo, *J. Mater. Chem. C*, 2020, **8**, 6640–6653.
- 16 Y. Fu, H. Zhu, J. Chen, M. P. Hautzinger, X. Y. Zhu and S. Jin, *Nat. Rev. Mater.*, 2019, **4**, 169–188.
- 17 H. Cho, S. H. Jeong, M. H. Park, Y. H. Kim, C. Wolf, C. L. Lee, J. H. Heo, A. Sadhanala, N. S. Myoung, S. Yoo, S. H. Im, R. H. Friend and T. W. Lee, *Science (80-.)*, 2015, **350**, 1222–1225.
- 18 J. H. Heo, S. H. Im, J. H. Noh, T. N. Mandal, C. S. Lim, J. A. Chang, Y. H. Lee, H. J. Kim, A. Sarkar, M. K. Nazeeruddin, M. Grätzel and S. Il Seok, *Nat. Photonics*, 2013, **7**, 486–491.
- 19 G. Xing, N. Mathews, S. Sun, S. S. Lim, Y. M. Lam, M. Grätzel, S. Mhaisalkar and T. C. Sum, *Science (80-.)*, 2013, **342**, 344–347.
- 20 J. Hwang, R. R. Rao, L. Giordano, Y. Katayama, Y. Yu and Y. Shao-Horn, *Science (80-.)*, 2017, **358**, 751–756.
- 21 Z. Wang, L. Yang, S. Liu, H. Yu, X. Li, Y. Xu, L. Wang and H. Wang, *Nanotechnology*, , DOI:10.1088/1361-6528/ab6fda.
- 22 X. Li, J. Wen, J. Low, Y. Fang and J. Yu, *Design and fabrication of semiconductor photocatalyst for photocatalytic reduction of CO₂ to solar fuel*, 2014, vol. 57.

- 23 P. M. Cox, R. A. Betts, C. D. Jones, S. A. Spall and I. J. Totterdell, *Nature*, 2000, **408**, 184–187.
- 24 wopfner and Kreuser, 1986, **0182**, 1–18.
- 25 C. S. S. R. Kumar, *Raman spectroscopy for nanomaterials characterization*, 2012, vol. 9783642206.
- 26 S. Anderson and A. Schade, 2009, 1955–1970.
- 27 C. S. Tedmon, H. S. Spacil and S. P. Mitoff, *J. Electrochem. Soc.*, 1969, **116**, 1170.
- 28 J. Zhang, *PEM fuel cell electrocatalysts and catalyst layers: Fundamentals and applications*, 2008.
- 29 G. T. Babcock, *Proc. Natl. Acad. Sci. U. S. A.*, 1999, **96**, 12971–12973.
- 30 I. Katsounaros, S. Cherevko, A. R. Zeradjanin and K. J. J. Mayrhofer, *Angew. Chemie - Int. Ed.*, 2014, **53**, 102–121.
- 31 Z. Zhang, J. Liu, J. Gu, L. Su and L. Cheng, *Energy Environ. Sci.*, 2014, **7**, 2535–2558.
- 32 H. A. Gasteiger, S. S. Kocha, B. Sompalli and F. T. Wagner, *Appl. Catal. B Environ.*, 2005, **56**, 9–35.
- 33 M. Shao, Q. Chang, J. P. Dodelet and R. Chenitz, *Chem. Rev.*, 2016, **116**, 3594–3657.
- 34 Q. He and E. J. Cairns, *J. Electrochem. Soc.*, 2015, **162**, F1504–F1539.
- 35 Y. Nie, L. Li and Z. Wei, *Chem. Soc. Rev.*, 2015, **44**, 2168–2201.
- 36 A. A. Gewirth and M. S. Thorum, *Inorg. Chem.*, 2010, **49**, 3557–3566.
- 37 P. G. Bruce, S. A. Freunberger, L. J. Hardwick and J. M. Tarascon, *Nat. Mater.*, 2012, **11**, 19–29.
- 38 L. Carrette, K. A. Friedrich and U. Stimming, *ChemPhysChem*, 2000, **1**, 162–193.
- 39 A. Kongkanand and M. F. Mathias, *J. Phys. Chem. Lett.*, 2016, **7**, 1127–1137.
- 40 J. Hui, S. Pakhira, R. Bhargava, Z. J. Barton, X. Zhou, A. J. Chinderle, J. L. Mendoza-Cortes and J. Rodríguez-López, *ACS Nano*, 2018, **12**, 2980–2990.
- 41 A. Damjanovic, M. A. Genshaw and J. O. Bockris, *J. Electrochem. Soc.*, 1967, **114**, 1107.
- 42 A. Damjanovic, D. B. Sepa and M. V. Vojnovic, *Electrochim. Acta*, 1979, **24**, 887–889.

- 43 H. S. Wroblowa, Yen-Chi-Pan and G. Razumney, *J. Electroanal. Chem. Interfacial Electrochem.*, 1976, **69**, 195–201.
- 44 K. I. Ozoemena, *RSC Adv.*, 2016, **6**, 89523–89550.
- 45 A. Athanassiou, M. I. Lygeraki, D. Pisignano, K. Lakiotaki, M. Varda, E. Mele, C. Fotakis, R. Cingolani and S. H. Anastasiadis, *Langmuir*, 2006, **22**, 2329–2333.
- 46 E. H. Yu, U. Krewer and K. Scott, *Energies*, 2010, **3**, 1499–1528.
- 47 W. Yuan, K. Scott and H. Cheng, *J. Power Sources*, 2006, **163**, 323–329.
- 48 B. Wang, *J. Power Sources*, 2005, **152**, 1–15.
- 49 R. M. Modibedi, M. K. Mathe, R. G. Motsoeneng, L. E. Khotseng, K. I. Ozoemena and E. K. Louw, *Electrochim. Acta*, 2014, **128**, 406–411.
- 50 X. M. Wang, M. E. Wang, D. D. Zhou and Y. Y. Xia, *Phys. Chem. Chem. Phys.*, 2011, **13**, 13594–13597.
- 51 H. J. Choi, S. M. Jung, J. M. Seo, D. W. Chang, L. Dai and J. B. Baek, *Nano Energy*, 2012, **1**, 534–551.
- 52 K. Nishanth, P. Sridhar, S. Pitchumani and A. Shukla, *ECS Trans.*, 2019, **28**, 273–281.
- 53 R. G. Motsoeneng, R. M. Modibedi, M. K. Mathe, L. E. Khotseng and K. I. Ozoemena, *Int. J. Hydrogen Energy*, 2015, **40**, 16734–16744.
- 54 W. Li, X. Zhao and A. Manthiram, *J. Mater. Chem. A*, 2014, **2**, 3468–3476.
- 55 E. Antolini, *Chempluschem*, 2014, **79**, 765–775.
- 56 J. K. Nørskov, J. Rossmeisl, A. Logadottir, L. Lindqvist, J. R. Kitchin, T. Bligaard and H. Jónsson, *J. Phys. Chem. B*, 2004, **108**, 17886–17892.
- 57 E. Antolini, *Energy Environ. Sci.*, 2009, **2**, 915–931.
- 58 K. Matsuki and H. Kamada, *Electrochim. Acta*, 1986, **31**, 13–18.
- 59 C. C. Chang, T. C. Wen and H. J. Tien, *Electrochim. Acta*, 1997, **42**, 557–565.
- 60 E. R. Vago and E. J. Calvo, *J. Electroanal. Chem.*, 1995, **388**, 161–165.
- 61 J. H. Kim, A. Ishihara, S. Mitsushima, N. Kamiya and K. I. Ota, *Electrochim. Acta*, 2007, **52**, 2492–2497.

- 62 S. Sharma and B. G. Pollet, *J. Power Sources*, 2012, **208**, 96–119.
- 63 Y. J. Wang, D. P. Wilkinson and J. Zhang, *Chem. Rev.*, 2011, **111**, 7625–7651.
- 64 L. Khotseng, A. Bangisa, R. M. Modibedi and V. Linkov, *Electrocatalysis*, 2016, **7**, 1–12.
- 65 J. Li, H. Zhou, H. Zhuo, Z. Wei, G. Zhuang, X. Zhong, S. Deng, X. Li and J. Wang, *J. Mater. Chem. A*, 2018, **6**, 2264–2272.
- 66 R. N. Singh, B. Lai and M. Malviya, *Electrochim. Acta*, 2004, **49**, 4605–4612.
- 67 E. Yeager, *J. Mol. Catal.*, 1986, **38**, 5–25.
- 68 H. L. Lord, W. Zhan and J. Pawliszyn, *Fundamentals and applications of needle trap devices*, 2012, vol. 2.
- 69 Y. Holade, N. E. Sahin, K. Servat, T. W. Napporn and K. B. Kokoh, *Catalysts*, 2015, **5**, 310–348.
- 70 K. -L. Hsueh, E. R. Gonzalez, S. Srinivasan and D. -T. Chin, *J. Electrochem. Soc.*, 1984, **131**, 823–828.
- 71 A. Damjanovic and V. Brusic, *Electrochim. Acta*, 1967, **12**, 615–628.
- 72 Z. X. Liang, T. S. Zhao, J. B. Xu and L. D. Zhu, *Electrochim. Acta*, 2009, **54**, 2203–2208.
- 73 T. Toda, H. Igarashi and M. Watanabe, *J. Electrochem. Soc.*, 1998, **145**, 4185–4188.
- 74 K. Tatsumi and R. Hoffmann, *J. Am. Chem. Soc.*, 1981, **103**, 3328–3341.
- 75 J. S. Griffith and P. R. S. L. A, *Proc. R. Soc. London. Ser. A. Math. Phys. Sci.*, 1956, **235**, 23–36.
- 76 J. P. Perdew, J. Tao, V. N. Staroverov and G. E. Scuseria, *J. Chem. Phys.*, 2004, **120**, 6898–6911.
- 77 W. Kohn, *Rev. Mod. Phys.*, 1999, **71**, 1253–1266.
- 78 J. A. Pople, *Rev. Mod. Phys.*, 1999, **71**, 1267–1274.
- 79 R. C. Ferrier, S. Pakhira, S. E. Palmon, C. G. Rodriguez, D. J. Goldfeld, O. O. Iyiola, M. Chwatko, J. L. Mendoza-Cortes and N. A. Lynd, *Macromolecules*, 2018, **51**, 1777–1786.
- 80 C. Sonkar, N. Malviya, R. Ranjan, S. Pakhira and S. Mukhopadhyay, *ACS Appl. Bio Mater.*, 2020, **3**, 4600–4612.

- 81 F. Paquin, J. Rivnay, A. Salleo, N. Stingelin and C. Silva, *J. Mater. Chem. C*, 2015, **3**, 10715–10722.
- 82 S. Pakhira, *RSC Adv.*, 2019, **9**, 38137–38147.
- 83 A. D. Becke, *J. Chem. Phys.*, 1992, **96**, 2155–2160.
- 84 N. Sinha, I. Deshpande and S. Pakhira, *ChemistrySelect*, 2019, **4**, 8584–8592.
- 85 R. Dovesi, A. Erba, R. Orlando, C. M. Zicovich-Wilson, B. Civalleri, L. Maschio, M. Rérat, S. Casassa, J. Baima, S. Salustro and B. Kirtman, *Wiley Interdiscip. Rev. Comput. Mol. Sci.*, 2018, **8**, 1–36.
- 86 Y. Lei, S. Pakhira, K. Fujisawa, X. Wang, O. O. Iyiola, N. P. López, A. L. Elías et al. *ACS Nano* 2017, **11**, 5103-5112.
- 87 N. R. Pradhan, C. Garcia, M. C. Lucking, S. Pakhira, J. Martinez, D. Rosenmann, R. Divan, A. V. Sumant, H. Terrones, J. L. Mendoza-Cortes, S. A. McGill, N. D. Zhigadlo and L. Balicas, *Nanoscale*, 2019, **11**, 18449–18463.
- 88 S. Pakhira and J. L. Mendoza-Cortes, *Phys. Chem. Chem. Phys.*, 2019, **21**, 8785-8796.
- 89 K. Sen, S. Pakhira, C. Sahu and A. K. Das, *Mol. Phys.*, 2014, **112**, 182–188.
- 90 S. Pakhira, T. Debnath, K. Sen and A. K. Das, *J. Chem. Sci.*, 2016, **128**, 621–631.
- 91 S. Pakhira, C. Sahu, K. Sen and A. K. Das, *Struct. Chem.*, 2013, **24**, 549–558.
- 92 S. Pakhira and J. L. Mendoza-Cortes, *J. Phys. Chem. C*, 2020, **124**, 6454–6460.
- 93 S. Pakhira, T. Debnath, K. Sen and A. K. Das, *Indian J. Chem. - Sect. A Inorganic, Phys. Theor. Anal. Chem.*, 2015, **54A**, 1369–1377.
- 94 K. Sen, B. Mondal, S. Pakhira, C. Sahu, D. Ghosh and A. K. Das, *Theor. Chem. Acc.*, 2013, **132**, 23–25.
- 95 S. Pakhira, K. P. Lucht and J. L. Mendoza-Cortes, *J. Phys. Chem. C*, 2017, **121**, 21160–21170.
- 96 R. Nagaraj, S. Pakhira, K. Aruchamy, P. Yadav, D. Mondal, K. Dharmalingm, N. Sanna Kotrappanavar and D. Ghosh, *ACS Appl. Energy Mater.*, 2020, **3**, 3425–3434.
- 97 N. Sinha and S. Pakhira, *ACS Appl. Electron. Mater.*, , DOI:10.1021/acsaelm.0c00867.
- 98 S. Pakhira, B. Mondal and A. K. Das, *Chem. Phys. Lett.*, 2011, **505**, 81–86.

- 99 D. Vilela Oliveira, J. Laun, M. F. Peintinger and T. Bredow, *J. Comput. Chem.*, 2019, **40**, 2364–2376.
- 100 P. Colinet, A. Gheeraert, A. Curutchet and T. Le Bahers, *J. Phys. Chem. C*, 2020, **124**, 8949–8957.
- 101 G. H. Kwei, A. C. Lawson, S. J. L. Billinge and S. W. Cheong, *J. Phys. Chem.*, 1993, **97**, 2368–2377.
- 102 K. Termentzidis, A. Pokropivny, M. Woda, S. Y. Xiong, Y. Chumakov, P. Cortona and S. Volz, *J. Phys. Conf. Ser.*, , DOI:10.1088/1742-6596/395/1/012114.
- 103 K. Hu, M. Wu, S. Hinokuma, T. Ohto, M. Wakisaka, J. I. Fujita and Y. Ito, *J. Mater. Chem. A*, 2019, **7**, 2156–2164.
- 104 K. Momma and F. Izumi, *J. Appl. Crystallogr.*, 2011, **44**, 1272–1276.
- 105 S. Pakhira, R. I. Singh, O. Olatunji-Ojo, M. Frenklach and W. A. Lester, *J. Phys. Chem. A*, 2016, **120**, 3602–3612.
- 106 S. Pakhira, K. P. Lucht and J. L. Mendoza-Cortes, *arXiv*.